Miner Deposita (2012) 47:383–410
DOI 10.1007/s00126-011-0378-z

ARTICLE

Metallogenic features of Miocene porphyry Cu and porphyry-related mineral deposits in Ecuador revealed by Re-Os, $^{40}Ar/^{39}Ar$, and U-Pb geochronology

Philip Schütte · Massimo Chiaradia · Fernando Barra · Diego Villagómez · Bernardo Beate

Received: 24 March 2010 / Accepted: 6 July 2011 / Published online: 30 July 2011

Abstract Mineralization and alteration events at ten Miocene porphyry Cu and porphyry-related epithermal mineral deposits in southern, central, and northern Ecuador were dated by means of molybdenite Re-Os, biotite and alunite $^{40}Ar/^{39}Ar$, and titanite U-Pb geochronology. Most of these hydrothermal events show a spatio-temporal correlation with porphyry intrusion emplacement as constrained by zircon U-Pb ages. The total age range for these events spans the 23.5–6.1 Ma period, without displaying systematic along- or across-arc age distribution trends. While epithermal deposits tend to be spatially associated with volcanic rocks of a similar age, porphyry Cu deposits in Ecuador are frequently spatially associated with deeper-seated basement units and batholith-scale precursor intrusive systems assembled over ≥5 m.y. time periods. In most cases, formation of the porphyry Cu deposits is related to the

Editorial handling: J. Perelló

Electronic supplementary material The online version of this article (doi:10.1007/s00126-011-0378-z) contains supplementary material, which is available to authorized users.

P. Schütte (✉) · M. Chiaradia · D. Villagómez
Department of Mineralogy, University of Geneva,
Rue des Maraîchers 13,
1205 Geneva, Switzerland
e-mail: Ph.Schutte@gmail.com

M. Chiaradia
e-mail: Massimo.Chiaradia@unige.ch

D. Villagómez
e-mail: Diego.Villagomez@gmail.com

F. Barra
Department of Geosciences, The University of Arizona,
Gould-Simpson Building, 1040 East Fourth St,
Tucson, AZ 85721, USA
e-mail: fbarrapantoja@ing.uchile.cl

B. Beate
Escuela Politecnica Nacional,
Quito, Ecuador
e-mail: bbeate@uio.satnet.net

Present Address:
P. Schütte
Federal Institute for Geosciences and Natural Resources (BGR),
Stilleweg 2,
30655 Hannover, Germany

Present Address:
F. Barra
Departamento de Geología, Universidad de Chile,
Plaza Ercilla 803,
Santiago, Chile

Present Address:
D. Villagómez
Tectonic Analysis Ltd., Chestnut House,
Burton Park, Duncton,
West Sussex GU28 0LH, UK

youngest magmatic (-hydrothermal) event in a given area, postdating batholith construction at a regional scale. The majority of Miocene deposits occurs in southern Ecuador where areally extensive, post-mineralization (late Miocene to recent) volcanic sequences with the potential to conceal mineralization at depth are lacking. Only few Miocene deposits occur in northern-central Ecuador, where they mainly crop out in the Western Cordillera, west of the productive present-day volcanic arc. The surface distribution of post-mineralization arc volcanism reflects along-arc variations in subducting slab geometry. Porphyry Cu and epithermal deposits in Ecuador define a Miocene metallogenic belt broadly continuous with its coeval counterpart in northern-central Peru. Although both belt segments were formed in an overall similar tectonomagmatic and metallogenic setting, their respective metal endowments differ significantly.

Keywords Mineral deposits · Porphyry Cu · Miocene metallogenic belt · Ecuador · Mineralization · Alteration · Geochronology

Introduction

Porphyry Cu and porphyry-related mineral deposits in the Andes of western South America typically occur in elongated metallogenic belts of several hundred (or even thousand) kilometers length, which regionally link deposits of a similar age range (Sillitoe 1988; Noble and McKee 1999; Sillitoe and Perelló 2005). Most of these deposits are intimately associated with arc magmatism resulting from the subduction of the Farallon/Nazca plate at the South American margin. Consequently, metallogenic belts tend to follow the overall spatio-temporal distribution of arc magmatism which is mainly dictated by the subducting slab geometry and upper plate structures (e.g., Sillitoe 1972; Kay et al. 1999; Richards 2003).

Metallogenic belts are best defined in the central Andes of southern Peru and northern-central Chile (ca. lat. 13–34° S) where Sillitoe and Perelló (2005) distinguish five major metallogenic epochs and associated Cu belts of late Paleozoic to early Mesozoic, middle to late Mesozoic, Paleocene to early Eocene, mid-Eocene to early Oligocene, and Miocene to early Pliocene age. Gold tends to be concentrated in discrete belts and districts as far as major deposits are concerned, although Au-rich porphyry Cu deposits contain significant quantities of both Au and Cu, and overlaps between both metals may exist for smaller-sized deposits (Sillitoe 2008). A Miocene metallogenic belt in northern and central Peru (lat. 6–13° S) hosts a number of world-class Cu and Au deposits (Sillitoe 1988; Noble and McKee 1999; Sillitoe and Perelló 2005). Metallogenic belts also occur in the northern Andes of Ecuador and Colombia (north of lat. 6° S), but have been less extensively studied than the metallogenic belts further south (Sillitoe and Perelló 2005, Sillitoe 2008).

Jurassic and, to a lesser extent, Tertiary (mostly Miocene) porphyry Cu ±Mo ±Au ±Ag and porphyry-related epithermal Au ±Ag ±Cu deposits contain the bulk of Ecuador's resources in Cu, Mo, Au, and Ag and form two distinct metallogenic belts (PRODEMINCA 2000a, b, c; Sillitoe and Perelló 2005; Chiaradia et al. 2009). A Jurassic metallogenic belt comprising, amongst others, the Fruta del Norte intermediate-sulfidation epithermal Au-Ag deposit (measured, indicated, and inferred resources of 4.1 Moz Au and 7.9 Moz Ag; Kinross Gold Corporation 2010), the Mirador porphyry Cu deposit (measured and indicated resources of 438 Mt at 0.61% Cu, 1.5 g/t Ag, 0.2 g/t Au, inferred resources of 235 Mt at 0.52% Cu, 1.3 g/t Ag, and 0.2 g/t Au; Corriente Resources Inc. 2008), and the Au-mineralized Nambija skarn field (>4 Moz Au "re-evaluated total resources"; PRODEMINCA 2000c) occupies an eastern, sub-Andean position in southern Ecuador (Figs. 1 and 2). A Miocene metallogenic belt spans the whole western Andean range and shows a broad continuity with the Miocene metallogenic belt of northern Peru and, possibly, with Miocene mineralization in southern Colombia (Fig. 2; Sillitoe 1988; PRODEMINCA 2000a, b; Sillitoe and Perelló 2005). Miocene mineralization types in Ecuador mainly comprise porphyry Cu ±Au ±Mo (e.g., Junín, Chaucha, and Gaby-Papa Grande; PRODEMINCA 2000a and references therein), high-sulfidation (e.g., Quimsacocha; PRODEMINCA 2000b; Beate et al. 2001), intermediate-sulfidation (e.g., Portovelo-Zaruma; Spencer et al. 2002), and low-sulfidation (e.g., Río Blanco; Bineli Betsi 2007; Ponce 2011) epithermal Au ±Ag ±Cu deposits. Although some of these deposits have a long-standing history of artisanal mineral production, partly since Inca times (in particular, Portovelo-Zaruma), many of Ecuador's Miocene mineral resources remain undeveloped to date (USGS 2009). The metal endowment of Miocene Ecuadorian mineral deposits (e.g., Table 1) seems to lag behind that of the Jurassic metallogenic belt in Ecuador (see above) as well as that of the neighboring Miocene Peruvian metallogenic belt (e.g., Noble and McKee 1999).

To date, magmatic and hydrothermal events associated with the Miocene metallogenic belt of Ecuador have mainly been constrained by means of K-Ar dating of

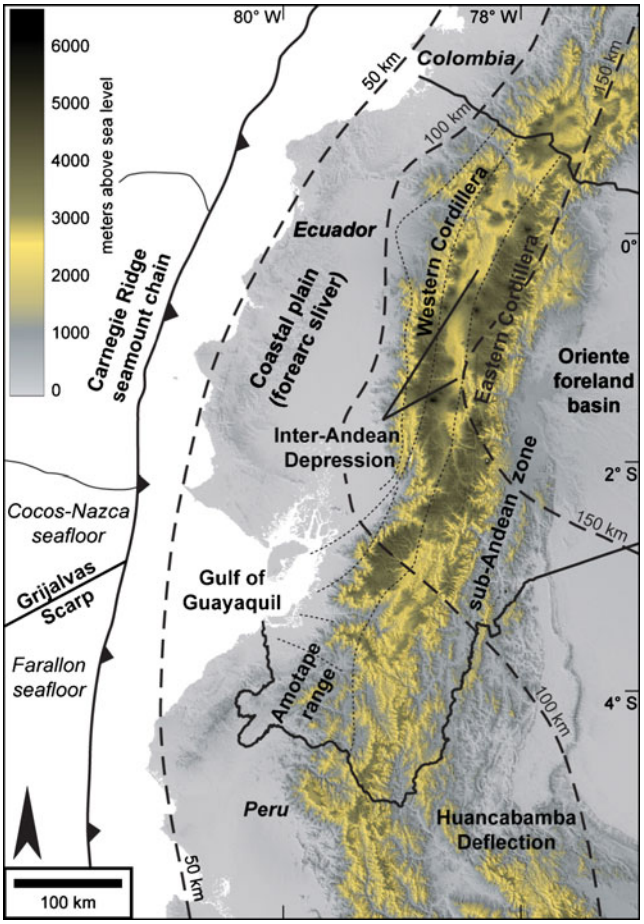

Fig. 1 Digital elevation map of Ecuador showing the major physiographic provinces defined by Litherland et al. (1994) as the Oriente foreland basin, the Eastern and Western Cordillera of northern-central Ecuador, separated by the Inter-Andean Depression (elevation between ca. 2,000–3,000 m a.s.l.; Winkler et al. 2005), and the coastal ("Costa") forearc sliver. Major faults or inferred faults (*thin dashed lines*; see Figs. 2 and 3 for details) approximately coincide with, though do not strictly correspond to, physiographic provinces in northern-central Ecuador. Also shown are Wadati-Benioff zones (*thick dashed lines*; Gutscher et al. 1999a, b; Guillier et al. 2001) outlining the subducting slab geometry. The Wadati-Benioff zone geometry below southern Ecuador and northern Peru has mostly been interpreted as indicating a flat slab segment, possibly related to the subduction of the inferred Inca oceanic plateau fragment (e.g., Gutscher et al. 1999b). Subduction of the Carnegie Ridge seamount chain at the northern-central Ecuadorian trench has contributed to minor slab shallowing (Guillier et al. 2001). Digital data obtained from the USGS Earth Resources Observation and Science Center; oceanic features from Lonsdale (2005)

either whole rock samples or K-bearing mineral concentrates (PRODEMINCA 2000a, b, and references therein). In this contribution, we present ten molybdenite Re-Os ages, four biotite and alunite $^{40}Ar/^{39}Ar$ ages, and a single titanite U-Pb age related to porphyry Cu and epithermal mineralization or alteration events from several late Oligocene to Miocene mineral deposits in southern, central, and northern Ecuador (Figs. 1, 2, and 3). Taken in combination with recently obtained zircon U-Pb ages of magmatic events at these deposits (Schütte et al. 2010a), the new data substantiate the geochronologic framework of the Miocene metallogenic belt of Ecuador, confirming the northwards continuity of the Miocene metallogenic belt of northern-central Peru (Sillitoe and Perelló 2005). Furthermore, the new data allow a closer inspection of the formation of porphyry Cu and porphyry-related mineral deposits in Ecuador, arc magmatism, and the associated geodynamic and tectonomagmatic setting.

Regional geology

From east to west, northern-central Ecuador comprises five major physiographic elements, namely the Oriente foreland basin, the NNE-trending Eastern and Western Cordilleras, separated by a number of elongated basins referred to as Inter-Andean Depression, and the coastal forearc region (Fig. 1; Litherland et al. 1994). In southern Ecuador, close to the Huancabamba Deflection, the main Andean (NNE) structural trend prevailing in northern-central Ecuador is disrupted where the Inter-Andean Depression swings west towards the Gulf of Guayaquil and an arc-transverse structural trend characterizes the northern end of the Amotape range (Fig. 1).

The Ecuadorian margin may be broadly divided into an eastern para-autochthonous province and a western allochthonous province. The two provinces are separated by a broad, NNE-trending suture zone concealed below Tertiary volcanic and sedimentary cover sequences of the Inter-Andean Depression; the western limit of the suture zone is likely represented by the major Calacalí-Pujilí-Pallatanga fault zone at the eastern border of the Western Cordillera (Figs. 1 and 2; Vallejo et al. 2009; Spikings et al. 2010). To the west of the suture zone, an allochthonous, late Cretaceous oceanic plateau sequence, accreted at ca. 75–70 Ma, forms the basement of the Ecuadorian forearc region and the Western Cordillera (e.g., Vallejo et al. 2009). The para-autochthonous province crops out to the east of the suture zone and comprises mostly Paleozoic to Mesozoic meta-sedimentary and (meta-) igneous basement units exposed in the Eastern Cordillera (Pratt et al. 2005); these units had originally been interpreted as a collage of different terranes (Litherland et al. 1994). It further includes broadly similar basement units of the Amotape range in

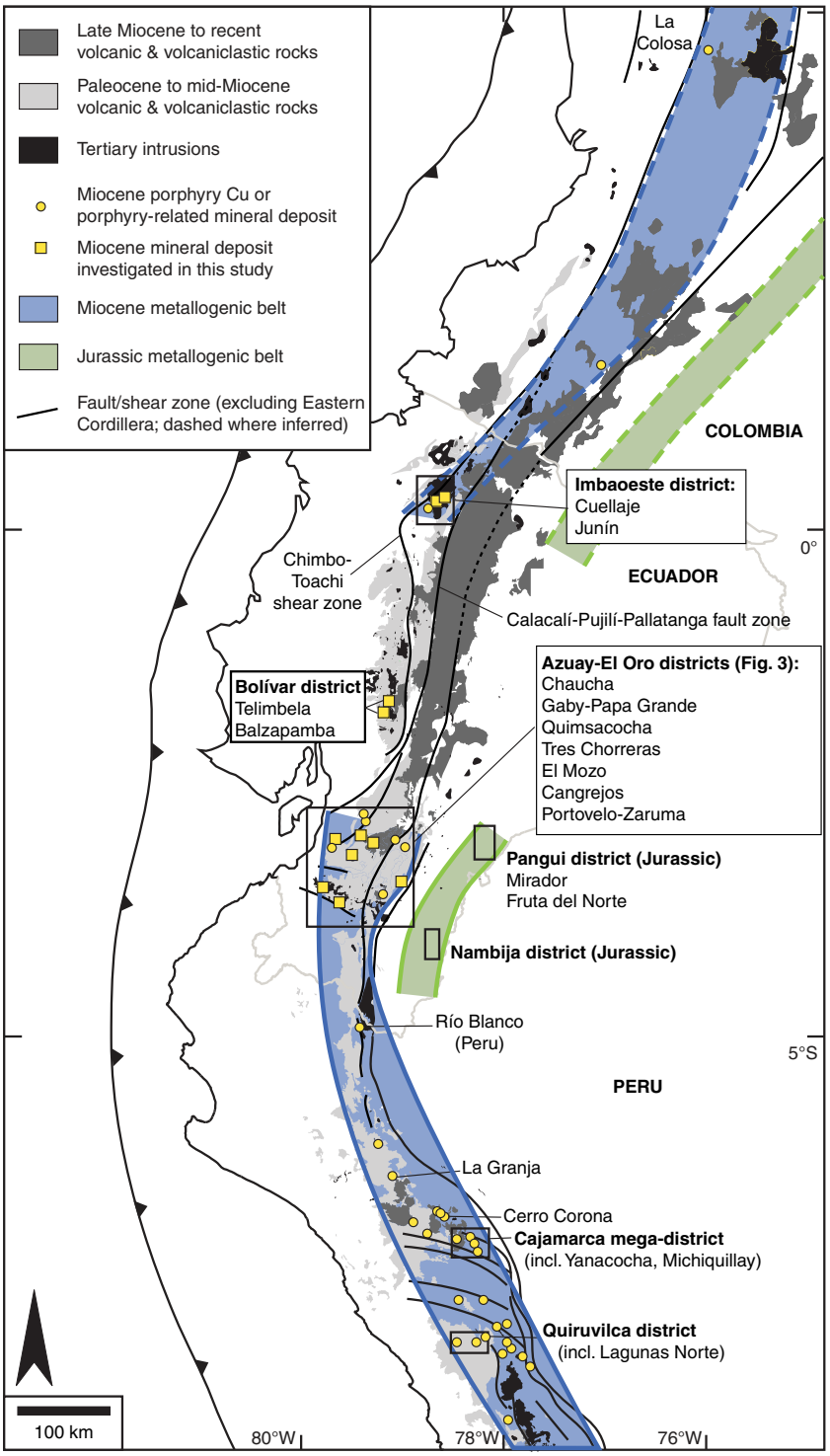

Fig. 2 Simplified geologic and metallogenic map of the NW South American margin showing the distribution of Tertiary arc magmatic units and the locations of Miocene (and, in Ecuador, minor late Oligocene) porphyry Cu and porphyry-related mineral deposits. These deposits define the semi-continuous Miocene metallogenic belt segments of northern-central Peru and southern Ecuador (Sillitoe 1988; Sillitoe and Perelló 2005). The northwards extension of the belt (through northern Ecuador and southern Colombia; dashed) is less well defined, as the density of deposits in this arc segment is lower than further south. Also shown is the Jurassic metallogenic belt of southern Ecuador (and its presumed location in southern Colombia; Sillitoe and Perelló 2005) hosting a number of giant deposits (e.g., the Fruta del Norte intermediate-sulfidation epithermal Au-Ag deposit and the Mirador porphyry Cu deposit). Deposit locations in Ecuador from PRODEMINCA (2000a, b, c). Deposit locations in northern Peru from Gustafson et al. (2004), Noble et al. (2004), and Sillitoe and Perelló (2005); additionally shown is the location of the Lagunas Norte deposit. Deposit locations in Colombia from Sillitoe and Perelló (2005); additionally shown is the location of the La Colosa deposit in central Colombia. Distribution of arc magmatic units and major structures in Ecuador from references compiled in Schütte et al. (2010a); major structures in Peru according to Mégard (1984) and McNulty et al. (1998); structures in the Eastern Cordillera are not shown

southern Ecuador (south of the Piñas-Portovelo fault; Figs. 2 and 3; Litherland et al. 1994).

Late Cretaceous to Eocene volcanic and volcaniclastic island arc sequences (dominated by the Macuchi Unit), erupted and deposited onto exotic oceanic plateau units, represent the dominant outcrop units in the Western Cordillera and its western foothills in northern-central Ecuador; these units are only locally covered by minor younger volcanic and sedimentary deposits. Further to the east, late Miocene to recent volcanic, volcaniclastic, and

sedimentary rocks crop out in the Inter-Andean Depression and, partly, the Eastern Cordillera. Several Tertiary intrusions are exposed in the Western Cordillera and tend to be aligned with broadly orogen-parallel fault zones of several hundred km of strike length (in particular, the Chimbo-Toachi shear zone; Fig. 2), which extend down to mid- and deep-crustal levels where they are defined by 35° east-dipping fault planes (Guillier et al. 2001). Miocene mineral deposits of the northern-central Ecuadorian Western Cordillera and its western foothills mostly represent porphyry Cu systems such as Junín, Telimbela, and Balzapamba which are spatially associated with Oligocene to Miocene intrusive centers of batholith dimensions (Fig. 2; PRODEMINCA 2000a; Schütte et al. 2010a).

Volcanic and volcaniclastic rocks of the Oligocene to early Miocene Saraguro Group constitute the major outcrop unit of the Tertiary arc assemblage in southern Ecuador, north of the arc-transverse trending Piñas-Portovelo fault (Fig. 3). These rock sequences are partly overlain by mid- to late Miocene volcanic formations as well as by volcaniclastic and sedimentary intramontane basin deposits; as in northern Peru, extensive late Miocene to recent volcanic cover sequences are absent in southern Ecuador (Figs. 2 and 3; Hungerbühler et al. 2002). The Saraguro Group and some of the younger rock sequences are punctured by a number of Tertiary intrusions and host several Miocene epithermal mineral deposits (e.g., Quimsacocha, El Mozo, and Portovelo-Zaruma) defining the Azuay and El Oro districts (Figs. 2 and 3; PRODEMINCA 2000a, b). Porphyry Cu (Chaucha) and porphyry Au-Cu deposits (Cangrejos) in this arc segment tend to be spatially associated with large Oligocene to Miocene intrusive centers in areas where the pre-Saraguro metamorphosed basement is exposed (Fig. 3). The Gaby-Papa Grande porphyry Au deposit at the southern end of the Western Cordillera is exclusively hosted by late Cretaceous, mafic oceanic plateau volcanic rocks (Fig. 3).

Tertiary geodynamic and tectonic setting at the Ecuadorian margin

Throughout the Tertiary, oblique plate convergence at the Ecuadorian margin between the Farallon/Nazca and the South American plates has been accommodated by a combination of oblique subduction slip and trench-parallel, dextral forearc sliver displacement along major orogen-parallel fault zones (Figs. 1 and 2); oblique subduction slip constitutes the dominant component at present (Daly 1989; Ego et al. 1996; Hungerbühler et al. 2002). Miocene compressive to transpressive pulses at 19 and 10–9 Ma are recorded by deformed intramontane basin deposits of the main arc region (Hungerbühler 1997; Hungerbühler et al. 2002), while opening of the Inter-Andean Depression as a ramp (and, locally, half ramp) basin has taken place in a transpressional setting since ca. 6 Ma (Winkler et al. 2005). These events tend to broadly correlate in time with compressive pulses recorded elsewhere in the Andes (e.g., northern-central Peru; Benavides-Cáceres 1999; Noble and McKee 1999).

The early Miocene breakup of the Farallon plate initiated the accretion of newly formed Nazca oceanic crust at the Cocos-Nazca spreading center (e.g., Lonsdale 2005). While subduction of older Farallon crust at the southern-central Ecuadorian margin continues to the present day, increasing proportions of younger Nazca crust have progressively been subducted at the northern Ecuadorian and Colombian margin since mid- to late Miocene times. The border between these two oceanic crustal domains is represented by the offshore Grijalvas Scarp progressively sweeping southwards along the margin (Fig. 1; Gutscher et al. 1999a; Lonsdale 2005).

The Carnegie Ridge seamount chain, formed at the Galapagos hotspot some 1,100 km west of the present-day Ecuadorian margin, is subducted at the northern-central Ecuadorian trench (Fig. 1). The exact timing of the probably late Miocene collision of this seamount chain with the Ecuadorian margin is still a matter of debate and complicated by jumps of the nearby Cocos-Nazca spreading center and seamount chain segmentation (Lonsdale and Klitgord 1978; Daly 1989; Gutscher et al. 1999a; Spikings et al. 2001; Witt et al. 2006). Ongoing late Miocene to Pliocene seamount chain subduction seems to have contributed to minor shallowing of the subducting slab below northern-central Ecuador, reflected by concomitant eastward frontal arc migration and arc broadening (Guillier et al. 2001; Schütte et al. 2010a).

Since mid- to late Miocene times, a flat slab geometry has been established below southern Ecuador and northern Peru, possibly in response to subduction of the inferred Inca oceanic plateau (Fig. 1; James and Sacks 1999; Gutscher et al. 1999b). The flat slab segment in southern Ecuador is associated with a gap in arc volcanism which progressively broadened northwards along the arc; active arc volcanism in Ecuador is restricted to the area north of latitude 2.5° S and late Miocene arc volcanic formations cover small areas between latitudes 2.5° and 4° S (Figs. 2 and 3; Beate et al. 2001; Schütte et al. 2010a).

Table 1 Geological and mineralogical features of Miocene Ecuadorian mineral deposits investigated in this study

Deposit	Country and host rocks	Intrusive units	Mineralization style	Tonnage and grade[a]	Observed characteristic features		Ref.[d]
					Alteration[b]	Mineralization[c]	
Junín	mainly basalt and turbidite units of the late Cretaceous Río Cala island arc sequence; mid-Miocene Apuela batholith	multiple hbl granodiorite porphyry dikes (9–6 Ma); hbl +bt-bearing granodiorite, tonalite and qtz-diorite/monzonite plutons of the Apuela batholith (19–12 Ma)	Cu-Mo porphyry; mainly (stockwork) veinlets and diss. hosted by porphyry dikes (and batholith units)	historic resource estimate (inferred resources): 982 Mt at 0.89% Cu, 1.9 g/t Ag, 0.04% Mo (0.4% Cu cutoff grade)	potassic: diss./repl. bt; qtz±kfs±mt veinlets; phyllic: diss./repl. ser (green and white), ill, chl, qtz, py, kao	potassic: qtz±cp±bn±mo veinlets; diss. cp-bn; phyllic: qtz-py±cp ±mo veinlets with ser halo	1–4
Telimbela	basaltic–andesitic lavas and siliceous–calcareous sediments of the (mostly) Eocene Macuchi Unit (island arc sequence); Telimbela batholith (Oligocene–Miocene)	multiple dikes and small stocks of hbl qtz-diorite porphyry; hbl/bt-bearing qtz-diorite, tonalite and granodiorite plutons of southern Telimbela batholith (ca. 26 and 21–15 Ma)	Cu (±Mo ±Au) porphyry; diss., veinlets, and hydroth. breccias hosted by porphyry intrusions and batholith plutons	no resource estimate available; individual assays show up to 1.65% Cu (hypogene) and 0.4 g/t Au	potassic: diss./repl. bt, mt, qtz, rt; sodic–calcic: ep, chl, act; hydroth. bx with bt and chl matrix; phyllic: ser, chl, qtz	potassic±sodic–calcic: qtz-cp-py ±mo veinlets and diss.; hydroth. bx with cp-py±mo diss. in matrix; phyllic: py-cp diss. and veinlets	1, 5
Balzapamba (El Torneado)	basaltic–andesitic lavas and siliceous–calcareous sediments of the (mostly) Eocene Macuchi Unit (island arc sequence); Balzapamba batholith (Oligocene–Miocene)	multiple hbl qtz-diorite porphyry dikes; hbl/bt-bearing qtz-diorite, tonalite and granodiorite plutons of northern Balzapamba batholith (ca. 34–30 and 26–21 Ma)	Cu (±Mo ±Au) porphyry (deeply eroded); diss. and veinlets hosted by bx batholith plutons, porphyry dikes, and, locally, Macuchi Unit	no resource estimate available; classified as low-grade (mostly <0.1% Cu), deeply eroded system	potassic: diss./repl./bx matrix of bt, ep, qtz, mt, rt, green ser, chl; locally associated with sodic–calcic: ep, chl, ab, act	potassic±sodic–calcic: qtz-cp-py ±mo veinlets (bx matrix) and diss.	1, 5, 6
Chaucha	pre-Tertiary metapelites; late Oligocene to early Miocene Saraguro Group volcanic rocks; mid-Miocene Chaucha batholith	multiple bt- and hbl-bearing granodiorite (±qtz-diorite) porphyry and qtz-diorite (seriate) stocks and dikes (ca. 10 Ma); bt-bearing granodiorite-tonalite plutons of the Chaucha batholith (ca. 15–10 Ma)	Cu-Mo porphyry; diss. and (stockwork) veinlets in porphyry intrusions and batholith plutons	historic resource estimate (sectors): *Naranjos*: 120 Mt at 0.4–0.5% Cu (0.3% Cu cutoff grade); *Gur-Gur*: 43.4 Mt at 0.54% Cu (0.4% Cu cutoff grade)	potassic: diss./repl. of bt, qtz, ep, mt; transitional potassic–phyllic: diss./repl./veinlets of qtz, ser (partly green), musc, kfs, bt, chl; phyllic: ser, ill, qtz, chl	potassic: diss. of cp (±bn); qtz-cp, qtz-mo, qtz-cp±mt±mo veinlets; transitional potassic–phyllic: diss. of cp; qtz-cp, qtz-mo, and qtz-py-cp±mo veinlets; phyllic: qtz-py-cp±mo veinlets (ser halo); supergene enrichment: cc, cov, Cu oxides	1, 7, 8
Gaby-Papa Grande	late Cretaceous oceanic plateau basalts (Pallatanga Unit)	multiple hbl-plag and plag-hbl porphyry stocks and dikes (ca. 21–20 Ma); tonalite (precursor) pluton	Au porphyry; porphyry-hosted diss. mineralization and (stockwork) veinlets, hydrothermal bx	measured and indicated resources: 308 Mt at 0.63 g/t Au (6.2 Moz), 0.09% Cu (0.4 g/t Au cutoff grade)	sodic–calcic: veinlets, diss./repl. and hydroth. bx with ab, act, chl, ep, ttn, mt, tm; potassic: hydroth. bx with qtz-bt matrix; phyllic: diss./repl. of ser, musc	sodic–calcic: veinlets, diss. and hydroth. bx with silicate-po-py-cp±mo; associated free Au reported; potassic: cp (bx matrix); phyllic: qtz-py±cp±po ±asp±gn±sl veinlets, partly with ser halo	1, 9
Quimsacocha	late Miocene andesitic tuffs/flows of the Quimsacocha Fm., ignimbrites of Turipamba Fm., volcaniclastic rocks of upper Turi Fm.	postmineral intra-caldera dacitic domes/plugs (7.1 Ma)	high-sulfidation epithermal Au-Ag-Cu mineralization associated with massive/vuggy silica bodies hosted by volcanic rock pile	probable reserves 8.1 Mt at 6.46 g/t Au (1.7 Moz), 36 g/t Ag, 0.42% Cu; measured and indicated resources: 2.1 Moz Au (3.0 g/t Au cutoff grade)	vuggy and massive silica bodies, with peripheral advanced argillic (alun, kao, dick, pyro) and argillic (ill, smec) alteration	late-stage mineralization: Au inclusions in late en; en sometimes associated with cov, postdating early py (I); possibly Au related to late pyrite (II)	10–12

Table 1 (continued)

Deposit	Country and host rocks	Intrusive units	Mineralization style	Tonnage and grade[a]	Observed characteristic features		Ref.[d]
					Alteration[b]	Mineralization[c]	
Tres Chorreras	late Oligocene silicic Saraguro Group volcanic rocks	several granodiorite–diorite intrusions? (strong pervasive alteration complicates distinction from silicic volcanic host rocks)	mineralized (diatreme) bx and polymetallic veins; epithermal Au (sulfidation state not constrained)	n/a	silicification and argillic alteration (associated with polymetallic veins): qtz, kao, ill, ser, chl, tm; bx matrix with jsp, mt, tm, hm	polymetallic veins: cp-mo-py-sl-gn; bx matrix: cp-mo-mt; Au-bearing qtz±py±gn±sl veinlets	1, 13
El Mozo	uppermost Saraguro Group dacitic–rhyolitic tuffs/flows (mid-Miocene)	pre-/synmineral (?) porphyry intrusion at depth (16 Ma)	high-sulfidation epithermal Au mineralization associated with vuggy silica bodies	inferred resources 3.5 Mt at 2.3 g/t Au (0.3 Moz; 0.5 g/t Au cutoff grade)	vuggy silica bodies with peripheral advanced argillic (alun, qtz) and argillic (ser, kao, chl) alteration	vuggy silica-hosted Au-bearing py veinlets and diss.; oxidized in places	12, 14
Cangrejos	Jurassic metasediments (Palenque Unit); Cangrejos-Zaruma intrusive belt	bt, hbl, and px-bearing qtz-diorite and diorite nested plutons (ca. 26 Ma), intruded by plag-hbl porphyry stocks and dikes	Au-Cu porphyry; mineralization is intrusion-hosted (diss., veinlets, partly bx)	historic resource estimate: "several 100 Mt" at 0.5–1.5 g/t Au, <0.2% Cu	sodic–calcic: diss./repl. and veinlets of ep, chl, mt, ab, act, qtz, tm; silicification	qtz±mt±cp±mo veinlets; cp±bn diss. (party associated with Au); Au-bearing qtz (-tm) veinlets	15
Portovelo-Zaruma	early Miocene Saraguro Group volcanic rocks (andesitic flows and tuffs)	multiple diorite and granodiorite intrusions (porphyry and seriate) to the north of Zaruma and in underground mine outcrops between Zaruma and Portovelo (24–20 Ma)	intermediate-sulfidation epithermal Au and base metal veins; porphyry Cu system(s) to the north of Zaruma	total production 1905–2002 of 4.5 Moz Au; measured and indicated resources at Portovelo: 2.4 Mt at 13.9 g/t Au (1.1 Moz)	porphyry—potassic: veinlets and diss. of bt, mt, qtz, tm. epithermal veins with argillic halo (ill, smec)	potassic: cp- and py-bearing qtz veinlets. epithermal: Au-bearing qtz- to cal-dominated veins with variable sl, gn, py, cp	1, 16

General abbreviations: *bx* breccia/brecciated, *diss.* disseminated/disseminations, *hydroth.* hydrothermal, *repl.* replacement; mineral abbreviations: *ab* albite, *act* actinolite, *alun* alunite, *asp* arsenopyrite, *bn* bornite, *bt* biotite, *cal* calcite, *cc* chalcocite, *cp* chalcopyrite, *chl* chlorite, *cov* covellite, *dick* dickite, *en* enargite, *ep* epidote, *gn* galena, *hbl* hornblende, *hm* hematite, *ill* illite, *jsp* jasperoid, *kao* kaolinite, *kfs* alkali feldspar, *mo* molybdenite, *mt* magnetite, *musc* muscovite, *po* pyrrhotite, *px* pyroxene, *py* pyrite, *pyro* pyrophyllite, *qtz* quartz, *rt* rutile, *ser* sericite, *sl* sphalerite, *smec* smectite, *ttn* titanite, *tm* tourmaline

[a] "Historic resource estimates" have not been verified by recent NI 43-101 or JORC-compliant methodology

[b] Only alteration styles associated with mineralization are listed; frequently observed propylitic alteration (mostly chl, ep), therefore, is not described in more detail

[c] The paragenetic positions of Au were generally not verified in this study. Reported Au occurrences are based on cited references

[d] References: 1—PRODEMINCA (2000a), 2—MICON (2005a), 3—MMAJ/JICA (1998), 4—Salazar (2007), 5—MMAJ/JICA (1991), 6—Chiaradia et al. (2004), 7—MICON (2005b), 8—Goossens and Hollister (1973), 9—Srivastava et al. (2008), 10—Iamgold (2009), 11—Beate et al. (2001), 12—PRODEMINCA (2000b), 13—Melling et al. (2007), 14—IBM (2005), 15—Potter (2004), 16—Spencer et al. (2002). Zircon U-Pb ages for associated intrusions are reported in Schütte et al. (2010a)

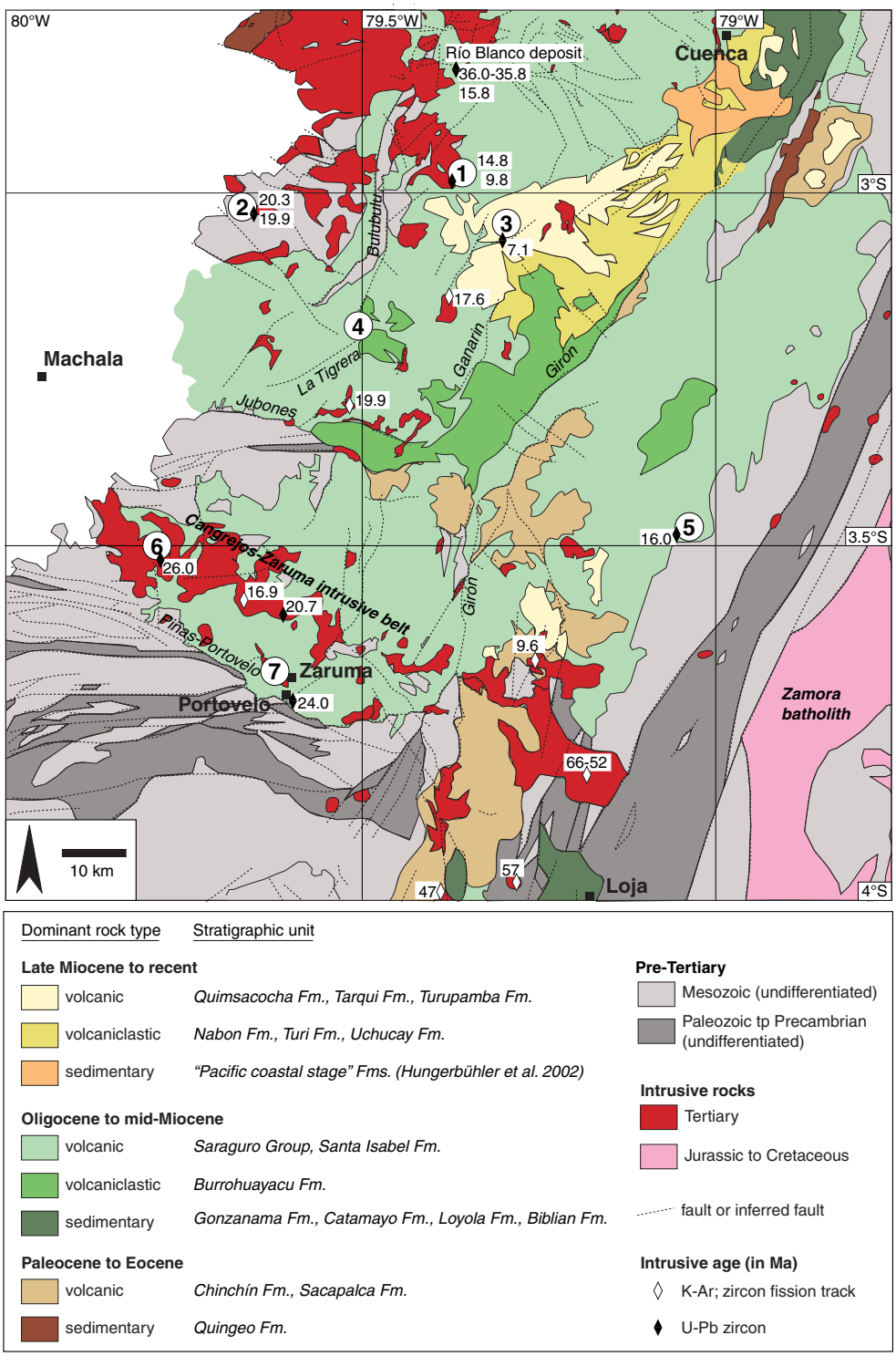

Fig. 3 Geological map of southern-central Ecuador showing the positions of late Oligocene to late Miocene mineral deposits investigated in this study. The names of major faults are indicated in italics on the map. Mineral deposits included in this study and shown on the map are: *1* Chaucha (porphyry Cu-Mo), *2* Gaby-Papa Grande (porphyry Au), *3* Quimsacocha (high-sulfidation epithermal Au-Ag-Cu), *4* Tres Chorreras (possibly porphyry-related breccias, polymetallic veins, and replacements; epithermal Au), *5* El Mozo (high-sulfidation epithermal Au), *6* Cangrejos (porphyry Au-Cu), *7* Portovelo-Zaruma (intermediate-sulfidation epithermal Au, possibly genetically related to porphyry Cu system). Magmatism of the major Zamora batholith is associated with the Jurassic metallogenic belt of Ecuador. Map adapted from Litherland et al. (1994), Pratt et al. (1997), and Dunkley and Gaibor (1997). Ages for intrusive rocks and events from Schütte et al. (2010a) and references therein (with additional Río Blanco ages by Bineli Betsi 2007; Ponce 2011)

Local geology and sampling details for investigated Miocene mineral deposits

We sampled six porphyry Cu and four porphyry-related (high- and intermediate-sulfidation epithermal) mineral deposits in northern, central, and mainly, southern Ecuador for Re-Os, $^{40}Ar/^{39}Ar$, and U-Pb geochronologic studies. The selection of mineral deposits to be included in the present study partly reflects their amenability for geochronologic investigations based on deposit type, the status of individual project development (e.g., drill core availability), and outcrop accessibility at the time of field work (2006–

2007), as well as the availability of reference data (in particular, PRODEMINCA 2000a, b). A number of additional mineral deposits of Tertiary age exist (e.g., the Fierro Urcu porphyry Cu and the Shyri epithermal Au deposit), but could not be included in this study due to logistic constraints. Overall, we aimed for a representative coverage of Miocene porphyry Cu and porphyry-related mineralization in Ecuador. The Río Blanco low-sulfidation epithermal Au-Ag deposit has been studied in detail elsewhere (Bineli Betsi 2007; Ponce 2011).

General geological and mineralogical features of investigated mineral deposits are summarized in Table 1, and some exemplary alteration and mineralization features are illustrated in Fig. 4. Sampling details, based on our macro- and microscopic investigations associated with sample selection for geochronologic analysis, are provided in Table 2 and Fig. 5. Throughout the course of this article, we employ the porphyry Cu alteration style definitions of Seedorff et al. (2005); this refers to potassic, transitional potassic–phyllic (as equivalent to potassic–sericitic), phyllic (as equivalent to sericitic), advanced argillic (which we do not differentiate further according to temperature), intermediate argillic, propylitic, silicic, and sodic–calcic alteration.

Geological maps are provided for a number of key mineral deposits where more detailed geochronologic studies were carried out (Figs. 6, 7, 8, and 9). Published geochronologic data for these deposits (Table 1), in conjunction with newly obtained geochronologic data, are discussed in detail in the Appendix (Online Resource 1). Throughout the course of this article, we always proceed from north to south when describing individual Ecuadorian mineral deposits.

Junín

The late Miocene Junín porphyry Cu-Mo deposit in northern Ecuador is hosted by the mid-Miocene Apuela batholith in the center of a NE-striking belt (subparallel to the Chimbo-Toachi shear zone; Fig. 2) of three porphyry Cu systems referred to as Imbaoeste district (MMAJ/JICA 1998; PRODEMINCA 2000a; MICON 2005a). Multiple pre-, syn-, and post-mineral hornblende granodiorite porphyry dikes of variable thickness strike NNE to ENE and dip 45–70° to the SE (Figs. 6 and 7; MICON 2005a; Salazar 2007). The porphyry dikes are similar in overall mineralogical composition, but display local textural variations where groundmass proportions vary from 30 to 80 vol.% and phenocryst sizes vary from relatively fine-grained (several millimeters in diameter) to coarse-grained (up to ca. 2 cm in diameter; Fig. 7; Salazar 2007). The porphyry dikes are hosted by seriate plutons forming part of the Apuela batholith, mostly representing biotite- and hornblende-bearing granodiorite, tonalite, quartz-diorite, and quartz–monzodiorite intrusions.

In the central part of the Junín deposit, porphyry Cu-Mo mineralization extends down to 600 m in depth. The mineralization is mainly represented by chalcopyrite-, bornite-, and molybdenite-bearing quartz and quartz–pyrite veinlets as well as disseminations of chalcopyrite and bornite; it is associated with zones of potassic and, to a lesser extent, phyllic alteration (phyllic alteration partly overprints potassic alteration; Figs. 4a and 7; Table 1). Propylitic alteration occurs in the peripheral parts of Junín and is also observed as overprint on potassic and phyllic alteration in the center of the deposit (Fig. 7; Salazar 2007). Alteration and mineralization affects both the porphyry dikes and the Apuela batholith; fluids preferentially exploited preexisting structures and lithologic contact zones (Salazar 2007). Postmineral porphyry intrusions (mainly occurring in peripheral parts of the deposit) show similar mineralogical and textural features as mineralized porphyry intrusions (Salazar 2007). Molybdenite for Re-Os dating was separated from quartz–molybdenite veinlets cutting through porphyry dikes with potassic alteration, subsequently overprinted by phyllic and, locally, propylitic alteration (Fig. 5a; Table 2); based on the nomenclature of Gustafson and Hunt (1975), this veinlet type has been classified as “B” by Salazar (2007).

Telimbela

The Telimbela and Balzapamba porphyry Cu (±Mo ±Au) systems define the Bolívar district in the western foothills of the central Ecuadorian Western Cordillera (Fig. 2; MMAJ/JICA 1991; PRODEMINCA 2000a). Porphyry Cu mineralization is spatially associated with parts of the Oligocene to mid-Miocene Telimbela and Balzapamba batholiths (mostly hornblende ± biotite-bearing granodiorite, tonalite, and quartz-diorite). Batholith units are emplaced into gently E-dipping, basic volcanic and volcaniclastic units of the Macuchi island arc sequence (MMAJ/JICA 1991).

Porphyry Cu (±Mo ±Au) mineralization at Telimbela occurs as several mineralized zones arranged in a broad NE trend, mostly centered on several NE-trending, early to mid-Miocene, partly porphyritic, hornblende-, and biotite-bearing quartz-diorite and granodiorite dikes and stocks in the southern portion of the Telimbela batholith. Individual dikes are few meters to tens of meters wide; broadly cylinder-shaped stocks display diameters up to 800 m (MMAJ/JICA 1991). Mineralization includes chalcopyrite-, pyrite-, and molybdenite-bearing quartz veinlets and disseminations of the same sulfides associated with potassic, sodic–calcic (Fig. 4g), and phyllic alteration, the latter as partial overprints on potassic assemblages (Table 1). The

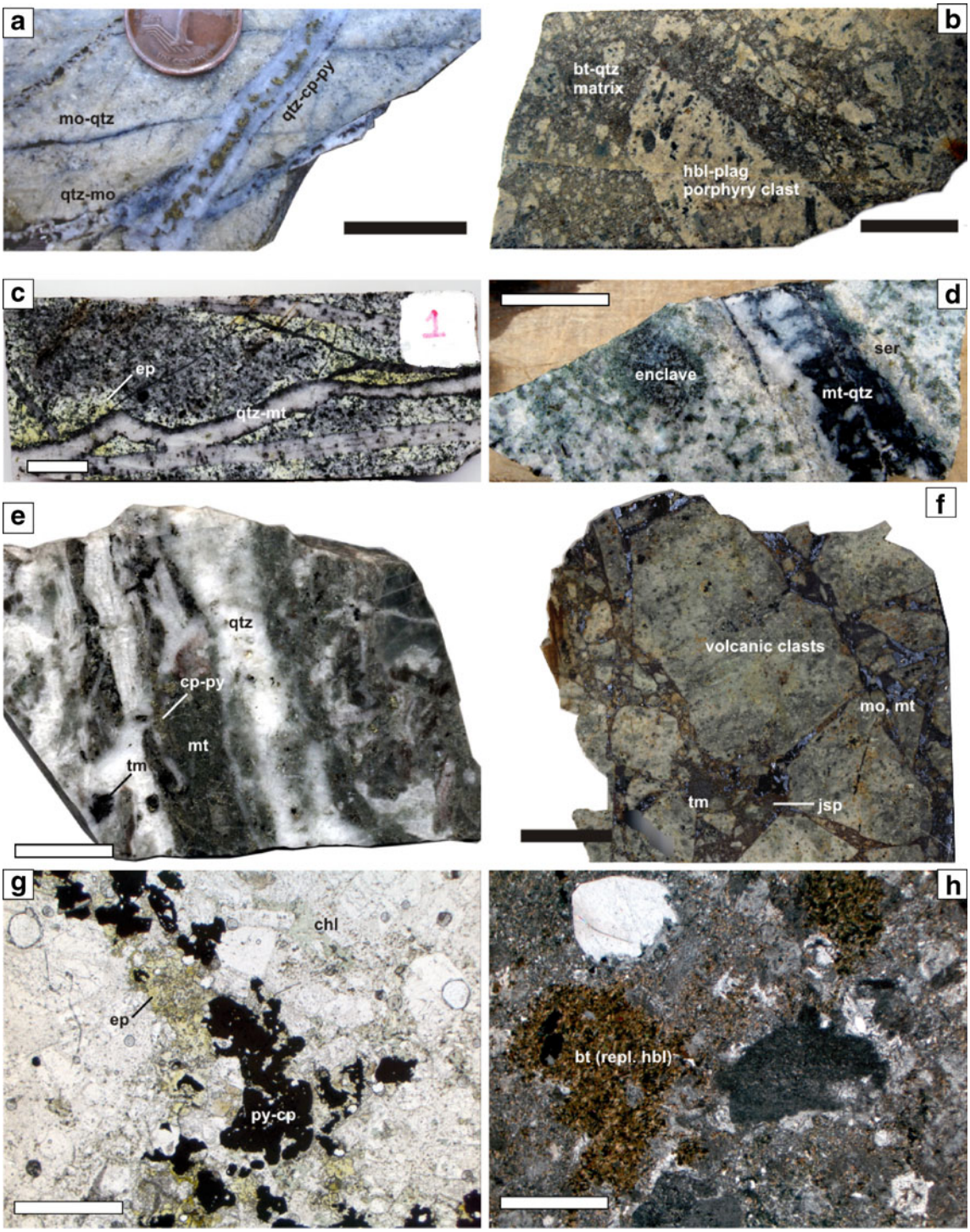

mineralization is hosted by all types of intrusions (including the batholith) and is locally also present in the Macuchi volcaniclastic host rocks. The geometry of the mineralized zones is poorly constrained, although drilling has shown mineralization to extend locally down to a depth of at least 200 m (MMAJ/JICA 1991). Hydrothermal brecciation (with chalcopyrite, pyrite, and molybdenite forming part of the biotite- and chlorite-bearing breccia matrix; Table 1) occurs around the contact zones of some intrusions, but is significantly less widespread than at the neighboring Balzapamba porphyry system (see below). We sampled batholith-hosted molybdenite–quartz veinlets associated with potassic alteration for Re-Os geochronology (Table 2).

◀ **Fig. 4** Typical alteration and mineralization features observed at porphyry Cu and porphyry-related mineral deposits investigated in this study (**a**–**f** macro-photographs, **g**–**h** micro-photographs); see Table 1 for more details. *Scale bar* is 2 cm for macro- and 1 mm for micro-photographs. **a** Hornblende granodiorite porphyry with pervasive potassic, overprinted by phyllic alteration and multiple quartz–molybdenite veinlets, cut by a quartz–chalcopyrite–pyrite veinlet (Junín). **b** Brecciated, subangular hornblende–plagioclase porphyry clasts cemented by mainly biotite and quartz (Gaby-Papa Grande). **c** Magnetite and quartz–magnetite veinlets with epidote haloes cutting plagioclase–hornblende porphyry with pervasive sodic–calcic alteration (Cangrejos). **d** Tonalite (Chaucha batholith) with pervasive potassic alteration (including magnetite–quartz veining) overprinted by phyllic alteration (Chaucha, Naranjos sector). **e** Andesite (Saraguro Group) cut by multiple tourmaline- and chalcopyrite/pyrite-bearing quartz-magnetite veinlets (part of a high-temperature, porphyry system to the north of Zaruma). **f** Breccia with subangular, silicified volcanic clasts and jasperoid–tourmaline–molybdenite–magnetite matrix (Tres Chorreras). **g** Hornblende-bearing quartz-diorite porphyry with pervasive sodic–calcic alteration, cut by epidote–pyrite–chalcopyrite veinlet (Telimbela). **h** Hornblende-bearing granodiorite porphyry with pervasive potassic alteration where biotite flakes completely replace hornblende phenocrysts and form "shreddy" disseminations in the porphyry groundmass (Chaucha, Gur-Gur sector). Mineral abbreviations used in the photographs: *bt* biotite, *chl* chlorite, *cp* chalcopyrite, *ep* epidote, *hbl* hornblende, *jsp* jasperoid, *mo* molybdenite, *mt* magnetite, *plag* plagioclase, *py* pyrite, *qtz* quartz, *tm* tourmaline

Balzapamba

The Balzapamba prospect area, situated within the northern part of the Oligocene to early Miocene Balzapamba batholith, comprises several exploration targets identified by MMAJ/JICA (1991) out of which we focus on the El Torneado target. Early Miocene porphyry Cu (±Mo ±Au) mineralization at El Torneado comprises chalcopyrite, pyrite, and molybdenite which occur as disseminations in batholith intrusions and, mainly, as part of the silicate–sulfide matrix (dominantly biotite, quartz, and chlorite) of a NE-trending, hydrothermally brecciated batholith body (Table 1). The up to 150-m-thick mineralized body dips SE 60° and shows an erratic internal distribution of Cu sulfides associated with potassic and, locally, sodic–calcic alteration (Table 1; MMAJ/JICA 1991). Phyllic assemblages overprint potassic alteration at levels close to the present-day surface, but they disappear at deeper levels (MMAJ/JICA 1991). A number of broadly NE-trending quartz-diorite porphyry dikes (few meters in thickness) display potassic alteration and mineralization, but their genetic relationship to the mainly batholith-hosted mineralization has not been constrained. A second, deeper-seated (>200 m depth) zone develops hydrothermal brecciation and associated low-grade Cu mineralization in batholith units, porphyry dikes, and Macuchi host rock (MMAJ/JICA 1991). This suggests that the El Torneado porphyry system integrates several distinct mineralization events, where the bulk of any potential mineralization has been lost to erosion. We sampled molybdenite associated with a potassic alteration assemblage related to the brecciated batholith (Table 2).

Chaucha

The late Miocene Chaucha porphyry Cu-Mo system is situated ca. 10 km to the east of the N- to NNE-trending Bulubulu fault system; it is mainly hosted by the SE portion of the mid-Miocene Chaucha batholith (Figs. 3 and 8). The Chaucha area contains a cluster of prospects and deposits of which Naranjos and Gur-Gur are thought to have the highest exploration potential (Fig. 8; MICON 2005b). Supergene enrichment blankets in these two sectors have been an initial target of several past exploration campaigns (e.g., by Ascendant Copper Corporation in 2007–2008); classic hypogene porphyry Cu mineralization is present at Naranjos but less obvious in other sectors (PRODEMINCA 2000a; MICON 2005b). Early exploration activities and geological studies at Chaucha are summarized by Goossens and Hollister (1973).

Mainly granodiorite porphyry dikes and stocks intrude the Chaucha batholith and, partly, older metamorphic basement rocks (Fig. 8). Hypogene mineralization is mainly associated with potassic and transitional potassic–phyllic alteration which affects several porphyry intrusions and parts of the adjacent Chaucha batholith (e.g., Naranjos; Figs. 4d, h and 5c; Table 1). The mineralization mostly comprises chalcopyrite-, pyrite-, and molybdenite-bearing quartz veinlets and disseminations within hydrothermally altered intrusions (Table 1). Intrusive and hydrothermal brecciation partly occurs at intrusive contacts and close to some fault zones (Fig. 8); it is not associated with appreciable mineralization (MICON 2005b).

Samples for geochronologic analysis were obtained from drill core material in the Naranjos and Gur-Gur sectors. A batholith-hosted quartz–molybdenite veinlet associated with potassic alteration, overprinted by transitional potassic–phyllic (±phyllic) alteration at Naranjos (Fig. 5c) and a porphyry-hosted quartz–pyrite–molybdenite veinlet associated with phyllic alteration at Gur-Gur were sampled for Re-Os analysis (Table 2). Additionally, biotite associated with pervasive potassic alteration affecting a porphyry dike in the Naranjos sector was sampled for $^{40}Ar/^{39}Ar$ geochronology (Table 2). The latter sample, biotite-bearing granodiorite porphyry with abundant fine-grained, "shreddy" biotite flakes in the porphyry groundmass, contains both magmatic ("book") and hydrothermal ("shreddy") biotite. The biotite K-Ar isotopic system (closure temperature range 280–345°C; e.g., Snee 2002) should principally be reset by high-temperature (often >500°C; e.g., Seedorff et al. 2005), porphyry-

Table 2 Description of samples used for Re-Os, $^{40}Ar/^{39}Ar$, and U-Pb geochronology of mineralization and alteration

Deposit/sample	Location/drill core	Description	Method
Junín			
E06194	35,050 N; 761,383 E 0° 19′ 1″ N, 78° 39′ 6″ W MJJ-29 at 305 m	hbl granodiorite porphyry (potassic, overprinted by phyllic ±propylitic alteration); qtz-mo (-cp) veinlet with fine-grained mo flakes	Re-Os mo
E06199	35,050 N; 761,383 E 0° 19′ 1″ N; 78° 39′ 6″ W MJJ-29 at 498 m	hbl granodiorite porphyry (potassic, overprinted by phyllic ±propylitic alteration); mo-qtz veinlets with coarse-grained mo flakes (Fig. 5a)	Re-Os mo
Telimbela			
E07037	9,817,260 N; 705,670 E 1° 39′ 9″ S; 79° 9′ 5″ W MJE-9 at 49 m	hbl-bearing tonalite (potassic, overprinted by propylitic alteration); multiple mo-qtz veinlets with coarse-grained mo flakes	Re-Os mo
Balzapamba			
E08003	9,808,050 N; 707,840 E 1° 44′ 9″ S; 79° 7′ 54″ W MJE-3 at 42 m	brecciated hbl granodiorite with matrix of bt, qtz, chl, rt including disseminated mo (fine-grained flakes), cp, py	Re-Os mo
Chaucha			
E07006 (Naranjos sector)	9,676,800 N; 676,140 E 2° 55′ 23″ S; 79° 24′ 55″ W NA-30 at 53 m	tonalite (potassic, transitional potassic–phyllic, and phyllic alteration) with qtz±cp, mt-cp-qtz-mo veining cut by qtz-mo vein with mo concentrated at vein margins (fine-grained mo flakes); in turn cut by musc-qtz-kfs±chl-cp-mo and py-cp-qtz veinlets; several veinlets with weak chl/ser halo (Fig. 5c)	Re-Os mo
E07002 (Naranjos sector)	9,677,350 N; 676,100 E 2° 55′ 5″ S; 79° 24′ 56″ W NA-26 at 224 m	bt-bearing granodiorite porphyry with potassic alteration (shreddy bt in matrix); selective ill±ep±chl alteration of plag phenos; bt (magmatic and hydrothermal) is mostly fresh and locally replaced by chl at microscopic scale[a]	$^{40}Ar/^{39}Ar$ bt
E06175 (Gur-Gur sector)	9,676,700 N; 677,800 E 2° 55′ 26″ S; 79° 24′ 1″ W core-5 at 80 m	granodiorite porphyry (phyllic alteration) with qtz-py-mo veinlet (fine-grained mo flakes), cut by qtz-py veinlet with ser halo	Re-Os mo
Gaby-Papa Grande			
E05075	9,661,850 N; 643,400 E 3° 3′ 31″ S; 79° 42′ 35″ W GD-08 at 151 m	hydrothermal breccia with altered (qtz-ser), subangular porphyry clasts; breccia matrix comprises qtz, po, cp±mo, and goe, hm, jar (later oxidation?); mo as fine-grained flakes	Re-Os mo
E05077	9,661,850 N; 643,400 E 3° 3′ 31″ S; 79° 42′ 35″ W GD-08 at 340 m	hbl-plag porphyry with strong pervasive Na-Ca alteration including act, chl, ep, ttn, and sulfides (mainly po); anhedral–euhedral ttn grains of ca. 50–500 μm size disseminated in porphyry groundmass (Fig. 5f)	U-Pb ttn
Quimsacocha			
E05103	9,663,557 N; 698,423 E 3° 2′ 33″ S; 79° 12′ 53″ W IQD-237 at 86 m	strongly silicified andesitic tuff; phenos completely replaced by alun needles (ca. 100 μm length) suggesting alun is of hypogene origin; alun grains are associated with py and frequently host rt inclusions (Fig. 5g)	$^{40}Ar/^{39}Ar$ alun
Tres Chorreras			
E07010	9,650,150 N; 663,591 E 3° 9′ 51″ S; 79° 31′ 40″ W	mineralized breccia with subangular clasts of altered volcanic rocks, matrix of jsp, mt (partly repl. by hm), mo, tm; coarse-grained mo flakes (Fig. 4f)	Re-Os mo
E07012	9,650,052 N; 663,543 E 3° 9′ 54″ S; 79° 31′ 42″ W	massive polymetallic vein with cp-mo-jsp-sl; host rock = completely replaced by clay minerals; mo as coarse-grained flakes (Fig. 5e)	Re-Os mo
El Mozo			
E07015	n/a; MDH-109 at 65 m	vuggy, completely silicified andesitic tuff; vug-filling py and coarse-grained alun (flakes several mm in length; Fig. 5b)	$^{40}Ar/^{39}Ar$ alun
Cangrejos			
E06065	9,614,000 N; 633,200 E 3° 29′ 29″ S; 79° 48′ 3″ W	bt-bearing qtz-diorite with weak pervasive Na-Ca alteration; qtz veinlets and a single mo-qtz veinlet (coarse-grained mo flakes; Fig. 5d)	Re-Os mo

Table 2 (continued)

Deposit/sample	Location/drill core	Description	Method
Zaruma			
E06114	9,600,028 N; 652,308 E 3° 37′ 3″ S; 79° 37′ 43″ W	plag-hbl porphyry (potassic, overprinted by propylitic alteration); phenos replaced by chl-ep, groundmass with abundant shreddy bt and disseminations of mt and cp; hydrothermal bt is mostly fresh (not replaced by chl)	$^{40}Ar/^{39}Ar$ bt

act actinolite, *alun* alunite, *bt* biotite, *chl* chlorite, *cp* chalcopyrite, *ep* epidote, *goe* goethite, *hbl* hornblende, *hm* hematite, *ill* illite, *jar* jarosite, *jsp* jasper-like silica, *kfs* alkali feldspar, *mo* molybdenite, *mt* magnetite, *po* pyrrhotite, *py* pyrite, *qtz* quartz, *rt* rutile, *ser* sericite, *sl* sphalerite, *tm* tourmaline, *ttn* titanite

[a] Only fresh biotite was handpicked for dating

related fluids causing potassic alteration as observed in this sample. To avoid problems with ^{39}Ar recoil for fine-grained hydrothermal biotite flakes (Snee 2002), we therefore concentrated coarse-grained magmatic biotite of this sample for geochronologic analysis and dating of the hydrothermal event.

Gaby-Papa Grande

The Gaby-Papa Grande porphyry Au deposit comprises multiple early Miocene porphyry and seriate intrusive stocks and dikes hosted by oceanic plateau basalts of the Pallatanga Unit (Fig. 9; PRODEMINCA 2000a; Srivastava et al. 2008). Potassic (Fig. 4b) and sodic–calcic (Fig. 5f) alteration associated with sulfide mineralization affects both porphyry intrusions (partly brecciated) and the mafic host rock; additional phyllic alteration occurs in the vicinity of the N-trending Tama fault (Table 1; Fig. 9). Srivastava et al. (2008) describe Au mineralization as being associated with sodic–calcic alteration (mostly as free Au), particularly well developed in previously fractured porphyry intrusions and in hydrothermal breccias which penetrate the porphyry intrusions; low-grade (<0.1%) Cu mineralization as chalcopyrite is reported as well (Table 1). We sampled molybdenite from a hydrothermal breccia matrix for Re-Os dating and hydrothermal titanite associated with porphyry-hosted sodic–calcic alteration for U-Pb analysis (Figs. 5f and 9; Table 2).

Quimsacocha

Quimsacocha constitutes a high-sulfidation epithermal Au-Ag-Cu deposit emplaced into a late Miocene volcanic and volcaniclastic rock sequence in southern Ecuador (Fig. 3). Subhorizontal massive and vuggy silica bodies with zoned advanced argillic and argillic alteration haloes host the Au-Ag-Cu mineralization introduced by late-stage fluids (mainly associated with enargite and second-generation pyrite; Table 1; Iamgold 2009). A number of postmineral dacitic plugs intrude the volcanic sequence (Beate et al. 2001); porphyry intrusions directly associated with mineralization have not been described. Consequently, while, for simplicity, we group Quimsacocha together with other porphyry-related deposits in this study, a direct porphyry link remains to be demonstrated. Hypogene alunite associated with advanced argillic alteration was sampled for $^{40}Ar/^{39}Ar$ geochronology (Fig. 5g; Table 2).

El Mozo

The mid-Miocene high-sulfidation epithermal Au deposit of El Mozo, situated at the border of the Eastern Cordillera, is hosted by a sequence of early to mid-Miocene volcanic and volcaniclastic rocks (Fig. 3). Gold mineralization at El Mozo, mainly associated with pyrite (Table 1), is hosted by vuggy silica bodies (with associated advanced argillic alteration) whose distribution seems to be controlled by multi-directional, high-angle faults (IBM 2005). Spatially associated intrusive units comprise granodiorite porphyry dikes (intersected in drill cores; partly showing argillic alteration) and surface outcrops of seriate diorite and granodiorite plugs. Hypogene alunite associated with advanced argillic alteration was sampled for $^{40}Ar/^{39}Ar$ geochronology (Fig. 5b; Table 2).

Tres Chorreras

Tres Chorreras constitutes a breccia pipe-related deposit emplaced at the northern end of the NE-trending La Tigrera fault; the mid-Miocene mineralization is hosted by Oligocene volcanic rocks of the Saraguro Group (Fig. 3; PRODEMINCA 2000a). Lithological units at Tres Chorreras include a pipe-shaped diatreme breccia body (ca. 600 m diameter at the surface) and a number of post-diatreme, irregularly shaped diorite and granodiorite plugs and dikes (PRODEMINCA 2000a; Melling et al. 2007). The breccia comprises subrounded to subangular juvenile clasts within a partly friable, variably mineralized rock flour matrix. Two

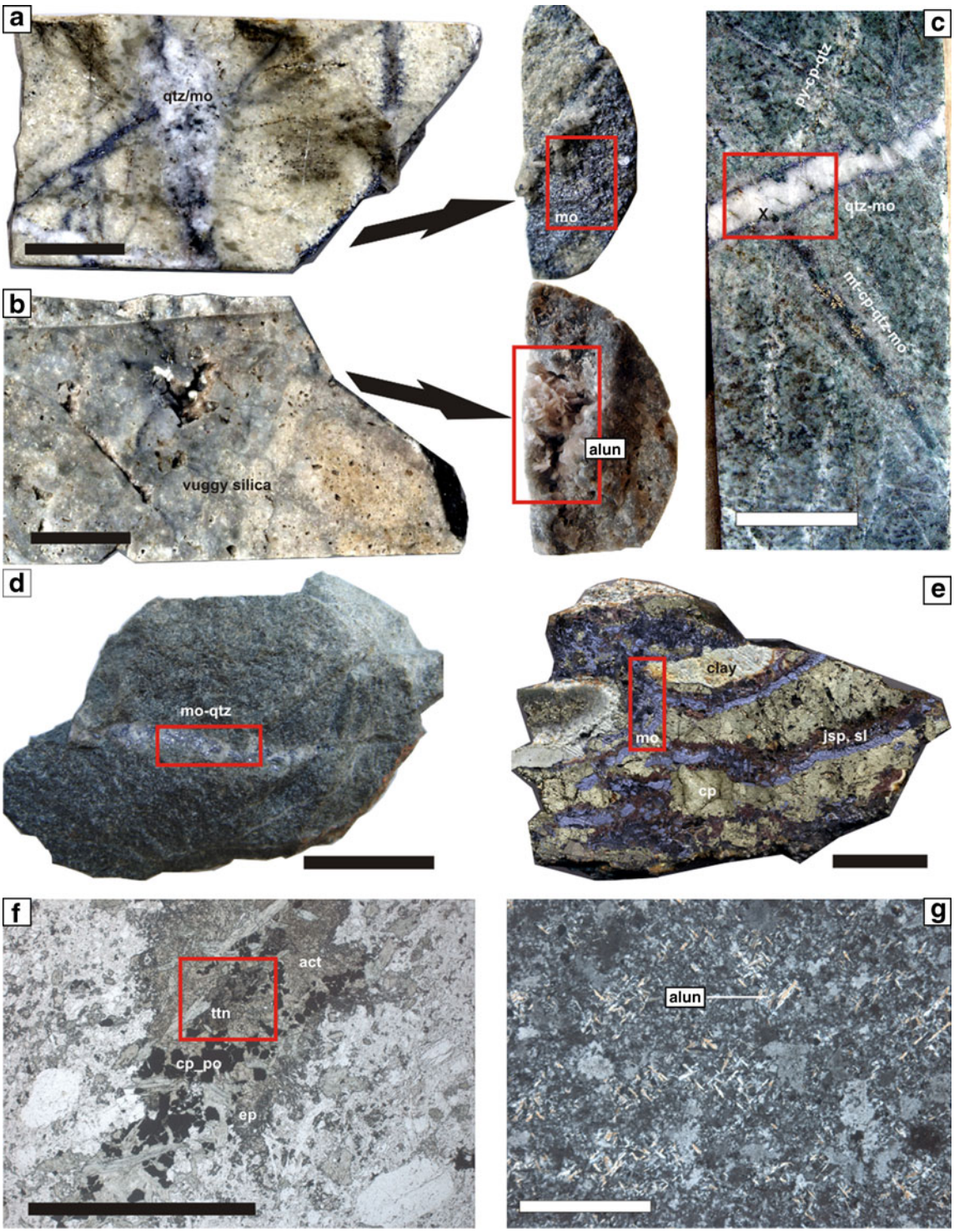

types of mineralization occur, namely polymetallic (possibly porphyry-related) and epithermal Au mineralization (Table 1; Melling et al. 2007). Polymetallic mineralization mainly occurs as veins, massive sulfide replacement bodies, and disseminations within the diatreme breccia body (Figs. 4f and 5e) and along the faulted contact between the diatreme breccia structure and a diorite intrusion. A set of NE-trending, subvertically dipping, epithermal Au-bearing quartz–base metal veinlets is also hosted by the diatreme breccia and a diorite intrusion (Melling et al. 2007). Widespread silicification and argillic alteration affects both the intrusions and the diatreme breccia; the

◀ **Fig. 5** Exemplary samples used for Re-Os, $^{40}Ar/^{39}Ar$, and U-Pb geochronology; see Table 2 for more details. *Scale bar* is 2 cm for macro-photographs (**a**–**e**) and separately noted below for micro-photographs (**f**–**g**); *red squares* mark areas with mineral selected for dating. **a** Hornblende granodiorite porphyry with pervasive potassic, overprinted by phyllic alteration, hosting multiple molybdenite–quartz veinlets (Junín). **b** Vuggy silica with partly fracture- and vug-filling, coarse-grained alunite flakes (advanced argillic alteration; El Mozo). **c** Tonalite hosting veinlets of early magnetite–chalcopyrite–quartz–molybdenite and quartz–molybdenite (molybdenite along veinlet margins was used for dating), cut by a thin molybdenite- and chalcopyrite-bearing muscovite–quartz–alkali feldspar–chlorite veinlet (marked as "X" in photograph) as well as multiple pyrite-chalcopyrite-quartz veinlets (with sericite halo); pervasive chlorite alteration. We interpret this succession as reflecting progressive overprinting of potassic, transitional potassic–phyllic, and phyllic alteration (Chaucha, Naranjos sector). **d** Quartz-diorite with pervasive sodic–calcic alteration and multiple quartz veinlets as well as a single veinlet of molybdenite–quartz (Cangrejos). **e** Banded chalcopyrite–molybdenite–jasperoid–sphalerite (polymetallic) vein, associated with pervasive argillic alteration (Tres Chorreras). **f** Micro-photograph of hornblende–plagioclase porphyry with sodic–calcic alteration including actinolite, epidote, chalcopyrite, pyrrhotite, and titanite (high relief); titanite from the same drill core and with similar paragenesis was used for U-Pb dating (Gaby-Papa Grande; 2 mm, *scale bar*). **g** Micro-photograph (crossed nicols) of silicified andesitic tuff with pervasive advanced argillic alteration where aggregates of alunite flakes (max. yellow-orange, first-order interference colors) replace former phenocrysts (Quimsacocha, 400 μm *scale bar*). Mineral abbreviations used in the photographs: *act* actinolite, *alun* alunite, *cp* chalcopyrite, *ep* epidote, *jsp* jasperoid, *mo* molybdenite, *mt* magnetite, *qtz* quartz, *po* pyrrhotite, *py* pyrite, *sl* sphalerite, *ttn* titanite

surface distribution of alteration zones has not been mapped (Melling et al. 2007). We sampled molybdenite from the breccia matrix (Fig. 4f) and as part of a polymetallic vein (Fig. 5e) for Re-Os analysis (Table 2).

Cangrejos

The late Oligocene to early Miocene Cangrejos porphyry Au-Cu system occurs at the western end of the Cangrejos-Zaruma intrusive belt (Fig. 3). It comprises multiple nested quartz-diorite and diorite plutons emplaced into Jurassic meta-sedimentary rocks, all intruded by a plagioclase–hornblende porphyry stock (ca. 1 km maximum diameter) as well as a number of variably oriented porphyry dikes; crackle breccia bodies are associated with several porphyry intrusions (Potter 2004). Gold–copper mineralization comprises chalcopyrite ± bornite disseminations associated with Au as well as chalcopyrite- and molybdenite-bearing quartz veinlets hosted by the intrusions. Locally, high-grade Au mineralization (up to 10–30 g/t) occurs within multi-directional quartz (-tourmaline) veinlets (Potter 2004). The mineralization is associated with sodic–calcic alteration and silicification partly affecting all intrusive lithologies as well as some breccia bodies (Table 1). We sampled a quartz–molybdenite veinlet cutting sodic–calcic altered quartz-diorite for Re-Os dating (Fig. 5d; Table 2).

Portovelo-Zaruma

Bracketed to the north and south by the eastern portions of the ESE-trending Cangrejos-Zaruma intrusive belt and the Piñas-Portovelo fault, respectively, the Portovelo-Zaruma mining district comprises multiple sets of broadly N-striking veins hosted by Oligocene to early Miocene volcanic rocks of the Saraguro Group (Fig. 3). Four vein sets, covering a total area of several tens of km^2, are separated by SE trending, dextral thrust faults dipping 40–60° SW (Spencer et al. 2002). Gold-bearing quartz–carbonate–base metal veins related to low-temperature fluids dominate the southern part of the vein system between Zaruma and Portovelo (Table 1). In contrast, veins to the north of Zaruma commonly contain tourmaline, magnetite, biotite, and quartz precipitated from high-temperature, possibly porphyry-related fluids (Fig. 4e; Table 1). The occurrence of these high-temperature veins, combined with observations of pervasive potassic alteration as well as advanced argillic alteration at higher topographical levels (the latter interpreted as part of a lithocap), prompted Spencer et al. (2002) to infer the presence of a porphyry system to the north of Zaruma, associated with a hydrothermal system that also affected vein formation further south. We sampled hydrothermal biotite related to the potassic alteration zone of a porphyry intrusion NW of Zaruma for $^{40}Ar/^{39}Ar$ geochronology (Table 2).

Analytical techniques

Pure molybdenite concentrates of 10–60 mg/sample were obtained from massive molybdenite or quartz–molybdenite veinlets, and from molybdenite disseminations in the matrix of hydrothermal breccias (Table 2, Fig. 5). Rhenium and Os were separated at the University of Arizona according to the procedures described in Barra et al. (2003, 2005). Samples were analyzed by negative thermal ionization mass spectrometry (Creaser et al. 1991) on a VG 54 mass spectrometer at the University of Arizona. Molybdenite ages were calculated using an ^{187}Re decay constant of 1.666×10^{-11} y^{-1} (Smoliar et al. 1996). Errors are reported at the 2-σ level and comprise the propagated uncertainties of the Re decay constant (0.31%), spike calibration for ^{185}Re (0.08%) and ^{190}Os (0.15%), as well as individual weighting and analytical random errors.

Sample selection for $^{40}Ar/^{39}Ar$ geochronology was based on microscopic studies to evaluate whether target minerals

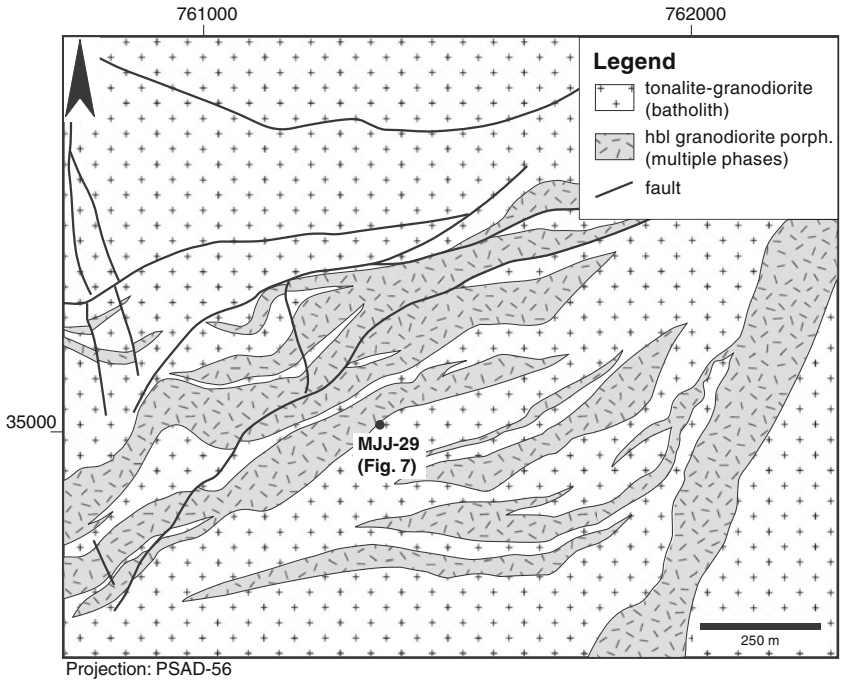

Fig. 6 Geological map of the Junín porphyry Cu-Mo system (MMAJ/JICA 1998). Porphyry dikes are hosted by the major early to mid-Miocene Apuela batholith. "MJJ-29" refers to the drill core shown in Fig. 7. Note that, due to security issues, field access was not possible at the time of study (2006–2007), such that the accuracy of the map could not be verified

of a specific sample were altered (in particular, chlorite replacing biotite, potentially causing ^{39}Ar recoil during subsequent sample irradiation; Snee 2002); in case alteration affected parts of a given sample, minerals showing alteration were removed by handpicking using a binocular. Purified mineral concentrates were irradiated for 15 h (alunite; samples E05103 and E07015) or 3 h (biotite; samples E06114 and E07002) in the TRIGA reactor at Oregon State University. Following sample irradiation, CO_2-IR laser incremental heating analysis at the University of Geneva was carried out on a multi-collector Argus GV Instruments mass spectrometer. Propagated systematic errors comprise decay constant, mass discrimination, and J value uncertainties. Weighted mean ages and cumulative ^{39}Ar release spectra were generated using the ArArCalc Excel macro of Koppers (2002). All errors are reported at the 2-σ level.

Hydrothermal titanite forms part of the sodic–calcic alteration assemblage at the Gaby-Papa Grande porphyry system (Table 2; sample E05077). Following dissolution of previously washed, multi-grain titanite fractions, U and Pb were separated using HCl-based anion exchange chromatography. Isotopic analyses at the University of Geneva were performed using a Thermo Fisher TRITON mass spectrometer equipped with a MasCom-2 electron multiplier and a digital ion counting system. The uncertainties of spike and blank Pb isotopic composition, mass fractionation correction, and tracer calibration were propagated to the final uncertainties of isotopic ratios and ages of each individual analysis. Uncertainties in the decay constants of ^{238}U and ^{235}U (Jaffey et al. 1971) were propagated separately and added quadratically to the weighted mean age. Concordia plots and weighted mean age calculations were prepared using the Isoplot v.3.31 Excel macro of Ludwig (2003). All uncertainties and error ellipses are reported at 2-σ levels, and the weighted mean ^{206}Pb/^{238}U age is presented at 95% confidence level.

Analytical techniques are described in more detail in the Appendix (Online Resource 2).

Results

Table 3 shows Re-Os data for the ten molybdenite concentrates analyzed in this study. Obtained ages fall in the latest Oligocene to late Miocene (23.5–6.1 Ma) age range. Total Re and ^{187}Os concentrations range between 35–1,019 ppm and 4.7–250 ppb, respectively. Rhenium–Osmium ages are supposed to closely approximate the timing of molybdenite precipitation (e.g., Chesley 1999).

Argon release patterns are shown in Fig. 10 and detailed results are listed in Table 4. All four analyzed samples are characterized by a high proportion of radiogenic Ar compared to trapped Ar. Therefore, we do not use inverse isochron plots for additional data evaluation, as data points tend to cluster close to the intercept with the ^{39}Ar/^{40}Ar axis, thus limiting the accuracy of trapped Ar compositions calculated based on the isochron (Kuiper 2002).

The analyzed biotite fractions (samples E06114, Zaruma, and E07002, Chaucha) display relatively little disturbed Ar release spectra allowing the definition of age plateaux

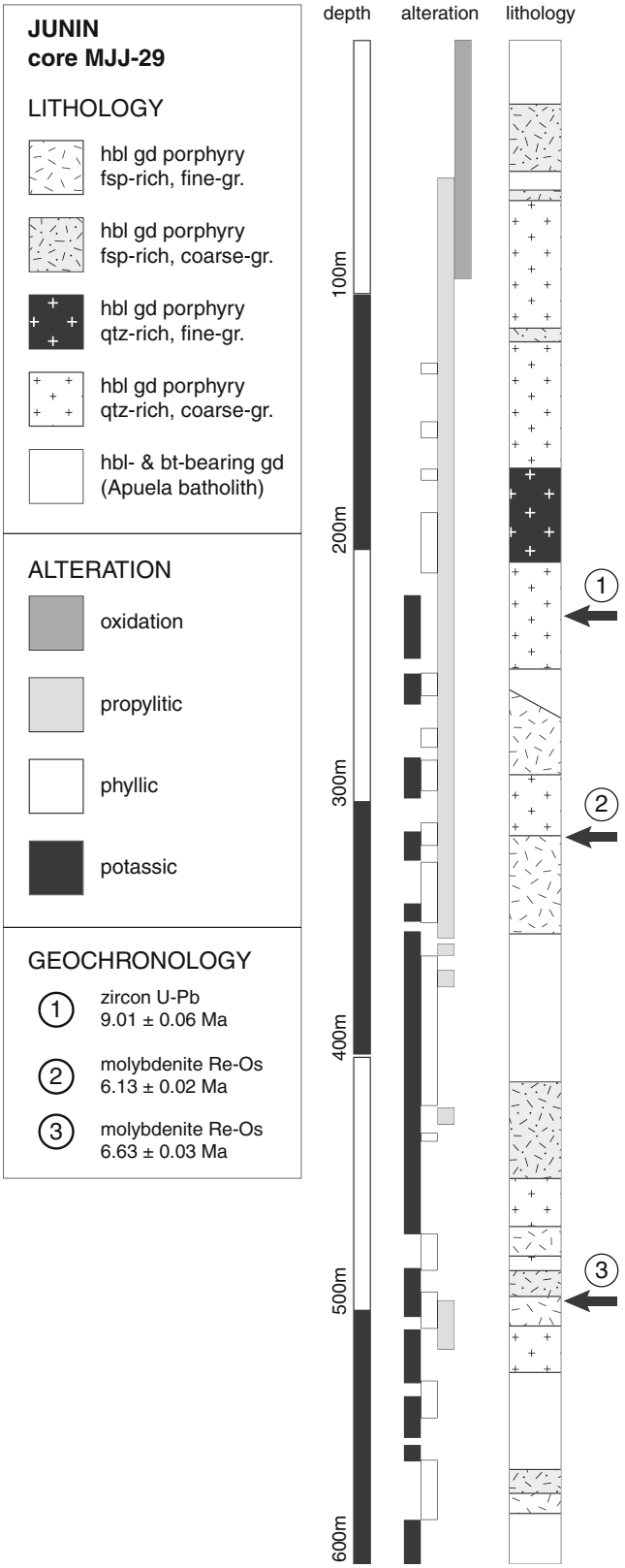

Fig. 7 Lithology and alteration drill core log of Junín core MJJ-29 (adapted from Salazar 2007) showing multiple porphyry intrusive phases and sampling locations for geochronologic study. The Apuela batholith (host rock) at nearby Cuellaje has a zircon U-Pb age of 12.87±0.05 Ma. U-Pb geochronologic data from Schütte et al. (2010a). Abbreviations: *bt* biotite, *coarse-gr.* coarse-grained, *fsp* feldspar, *fine-gr.* fine-grained, *gd* granodiorite, *hbl* hornblende, *qtz* quartz

(following the terminology of Knight et al., 2003, where a plateau comprises five or more successive heating steps not showing a resolvable slope, representing >50% of the total released ^{39}Ar, and concordant within 2-σ errors) at 19.15± 0.18 Ma (Zaruma; Fig. 10a) and 10.6±0.3 Ma (Chaucha; Fig. 10b). Significantly younger apparent ages in the low-temperature heating steps of sample E06114 (Fig. 10a) are interpreted as Ar loss, possibly related to minor (submicroscopic) biotite alteration. The closure temperature range for Ar diffusion in biotite is 345–280°C (Snee 2002) implying that the ^{40}Ar/^{39}Ar age obtained at Zaruma should reflect cooling after biotite precipitation from higher-temperature fluids causing potassic alteration.

Minor Ar loss in the low-temperature heating steps of sample E07002 from Chaucha (Fig. 10b) is not clearly analytically resolvable such that we include these steps in the plateau age whose MSWD is near unity, i.e., statistically acceptable. However, as noted above, this sample represents magmatic biotite whose K-Ar isotopic system is tentatively suspected to be reset by the high-temperature hydrothermal event causing potassic alteration. The somewhat younger apparent ^{40}Ar/^{39}Ar ages obtained from the low-temperature heating increments indicate that thermal resetting might not have been complete. Therefore, the 10.6±0.3 Ma age should be considered as a maximum age for the hydrothermal potassic alteration event at Chaucha.

The analyzed alunite fractions (samples E05103, Quimsacocha, and E07015, Zaruma) show strongly disturbed Ar release spectra and the samples do not define acceptable age plateaux. An “apparent plateau” can be approximated for sample E05103 (Quimsacocha) with an age of 9.5±0.5 Ma, albeit only representing 42% of the total released ^{39}Ar (Fig. 10c; Table 4). This apparent plateau age overlaps within error with the total fusion age of 9.0±0.3 Ma, and we thus consider it as a first-order geologically meaningful estimate for cooling below the alunite Ar closure temperature range (210–200°C; Snee 2002) following advanced argillic alteration and alunite formation at Quimsacocha.

The total fusion age for El Mozo alunite (E07015) is 16.9±0.2 Ma; the strongly disturbed Ar release spectrum does not allow definition of an age plateau (Fig. 10d). While analyzed, alunite was fresh and its grain size (several millimeter-sized flakes; Table 2; Fig. 5b) coarser than the range where ^{39}Ar recoil is commonly expected to be significant (<10 μm; Snee 2002), we suspect that the disturbed Ar release spectrum is partly due to ^{39}Ar recoil,

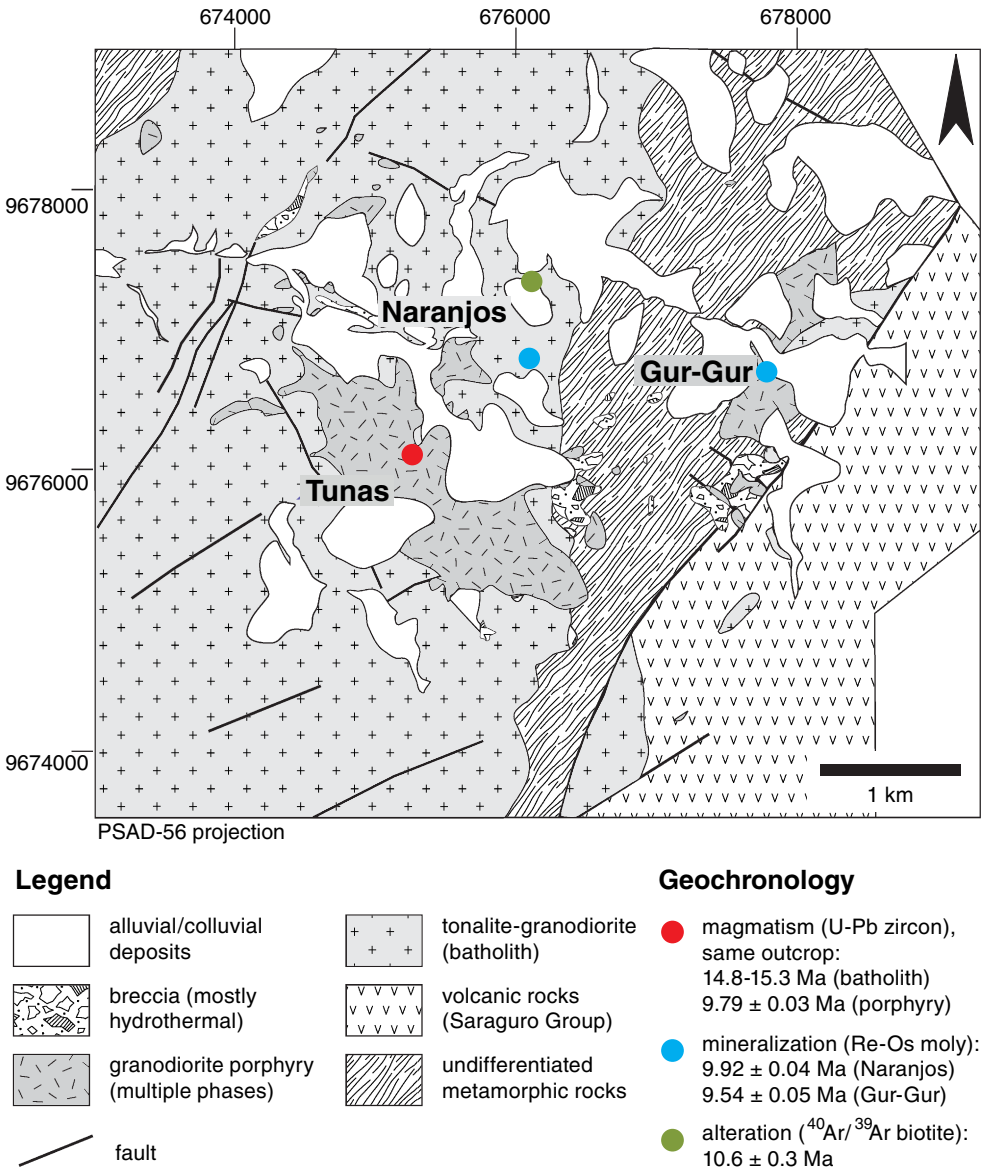

Fig. 8 Geological map of the Chaucha Cu-Mo porphyry district (after MICON 2005b). Sampling locations for Re-Os and ^{40}Ar/^{39}Ar geochronology refer to drill core sites (Table 2); samples for zircon U-Pb dating of intrusive units in the Tunas sector (Chaucha batholith and porphyry) were obtained from the same outcrop (Schütte et al. 2010a)

either between alunite and alunite-hosted mineral or fluid inclusions, across individual alunite crystal structural boundaries, or out of the non-encapsulated irradiation package, the latter potentially causing an age overestimation (Spikings et al. 2010). In addition, heterogeneously distributed excess Ar might further contribute to the disturbed age spectrum. The geological relevance of the El Mozo alunite age is thus uncertain.

Hydrothermal titanite associated with sodic–calcic alteration at the Gaby-Papa Grande porphyry system yields a weighted mean ^{206}Pb/^{238}U age of 20.17±0.16 Ma (Fig. 11, Table 5). Significant scatter among individual-fraction titanite ^{207}Pb/^{235}U ages suggests a partly imperfect characterization of the titanite common Pb (Pb$_c$) isotopic composition, but the homogeneous distribution of ^{206}Pb/^{238}U ages implies that ^{206}Pb/^{238}U age systematics were not significantly affected by this issue (Fig. 11). The expected temperature range of early magmatic sodic–calcic alteration as observed at Gaby-Papa Grande (Srivastava et al. 2008) is supposed to be close to or below the closure temperature range of titanite with respect to the U-Pb isotopic system (up to 720–780°C for rapid cooling rates; Schmitz and Bowring 2001). Therefore, the U-Pb titanite age should closely correspond to the timing of titanite formation associated with sodic–calcic alteration.

Discussion

Spatio-temporal distribution patterns of Miocene mineralization and magmatism in Ecuador

The geochronologic data presented above, in conjunction with recently obtained zircon U-Pb ages on magmatic

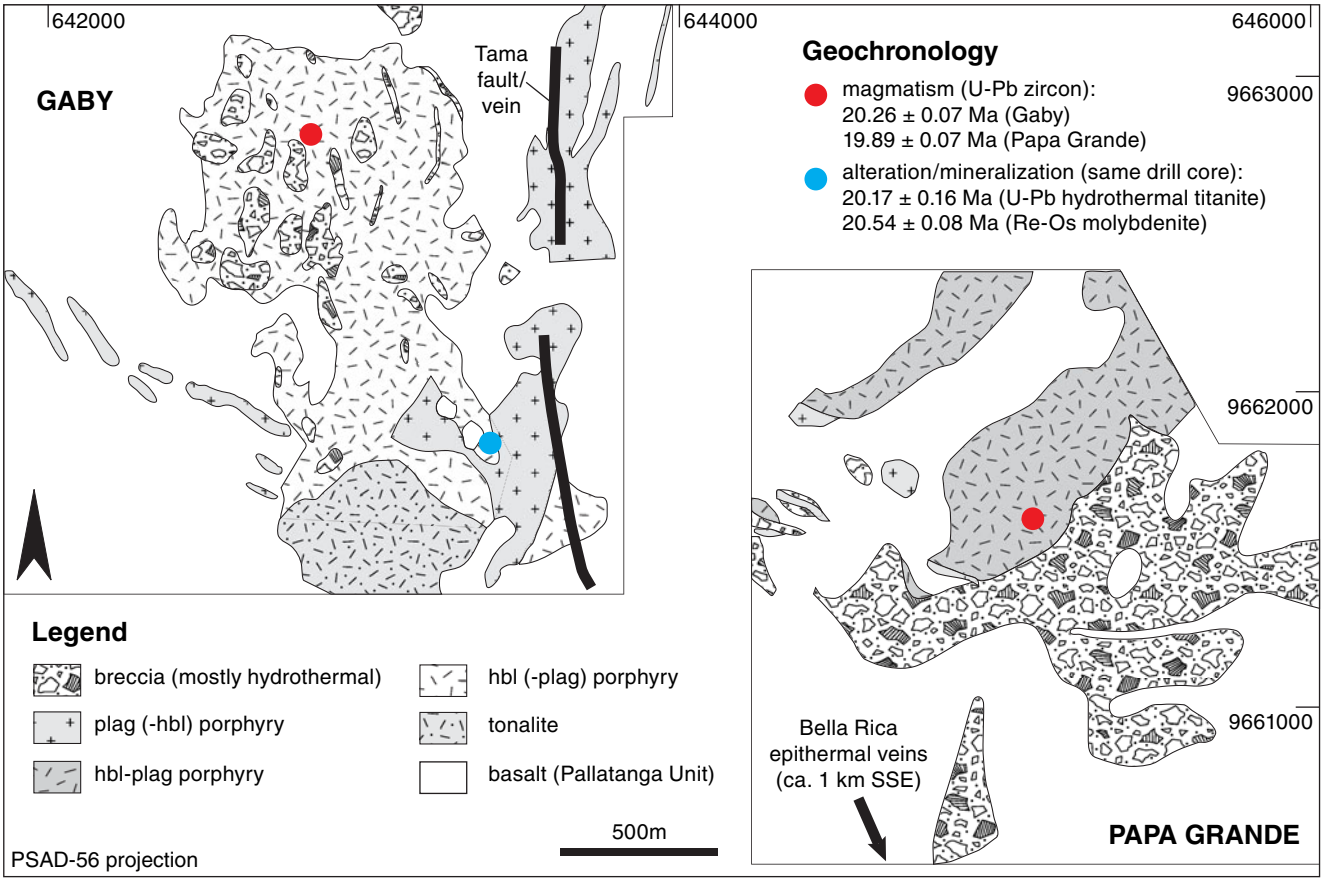

Fig. 9 Geological map of the Gaby-Papa Grande porphyry Au system and sampling locations for geochronology. Samples for zircon U-Pb dating of intrusive units (Schütte et al. 2010a) were collected from surface outcrop exposures whereas samples used for molybdenite Re-Os and titanite U-Pb geochronology represent drill core material (Table 2). Map adapted from Srivastava et al. (2008). Abbreviations: *plag* plagioclase, *hbl* hornblende

events from Miocene Ecuadorian porphyry Cu and porphyry-related mineral deposits (Schütte et al. 2010a) as well as previously published K-Ar data (e.g., PRODEMINCA 2000a, and references therein), are herein used to constrain the regional-scale spatio-temporal distribution patterns of Miocene mineralization associated with arc magmatism in Ecuador. A more detailed discussion of geochronologic data with respect to individual mineral deposits is given in the Appendix (Online Resource 1).

General tectonomagmatic features of the Miocene metallogenic belt of Ecuador are broadly in agreement with observations elsewhere in the Andes (e.g., Sillitoe and Perelló 2005; Sillitoe 2010, and references therein). Alteration and mineralization events, covering a total age range of 23.5 to 6.1 Ma, closely correlate in time and space with porphyry intrusion emplacement at most mineral deposits. Several of the porphyry Cu deposits and prospects in Ecuador are spatially associated with precursor intrusive systems of batholith dimensions assembled over a time period of several m.y. (ca. 5 m.y. at Chaucha; >5 m.y. at Junín, Telimbela, and Balsapamba; Fig. 12; Schütte et al. 2010a). At a given location, porphyry Cu deposit formation is frequently associated with the youngest magmatic event and postdates major batholith construction (Fig. 12). Significantly older basement units may be exposed at the deposit to district scale (e.g., at Gaby-Papa Grande, Chaucha, and Cangrejos). Porphyry Cu mineralization in Ecuador is often hosted by both porphyry and precursor intrusions (e.g., at Junín) and, to a lesser extent, may also include older wall rocks (e.g., at Gaby-Papa Grande).

Coeval volcanic rocks are not observed in direct spatial association with Ecuadorian porphyry Cu deposits, although they do occasionally occur at a regional scale (Table 1; Fig. 12). In contrast, most high- and intermediate-sulfidation epithermal deposits included in this study (Quimsacocha, El Mozo, and Portovelo-Zaruma) are hosted by volcanic rocks which are not significantly older (few m.y. at most) than the mineralization itself (Table 1); batholith-scale plutonic centers are not exposed in direct spatial association with these epithermal deposits. At the Río Blanco low-sulfidation epithermal deposit, the major-

Table 3 Re-Os data for molybdenite of Miocene Ecuadorian mineral deposits

Deposit/sample	Weight [mg]	Total Re [ppm]	^{187}Re [ppm]	^{187}Os [ppb]	Age±2-σ [Ma]
Junín					
E06199	39	294.4 (2)	184.3 (2)	18.83 (3)	6.13±0.02
E06194	16	408.8 (3)	255.9 (2)	28.28 (5)	6.63±0.03
Telimbela					
E07037	60	312.8 (3)	195.8 (2)	62.56 (9)	19.17±0.07
Balzapamba					
E08003	14	580.1 (5)	363.1 (3)	130.4 (2)	21.50±0.08
Chaucha					
E07006	30	354.6 (3)	222.0 (2)	36.68 (6)	9.92±0.04
E06175	11	70.44 (6)	44.10 (4)	7.01 (1)	9.54±0.05
Gaby-Papa Grande					
E05075	44	442.9 (4)	277.3 (2)	94.9 (1)	20.54±0.08
Tres Chorreras					
E07010	55	641.0 (5)	401.3 (3)	86.4 (1)	12.93±0.05
E07012	52	35.29 (3)	22.09 (2)	4.693 (8)	12.75±0.06
Cangrejos					
E06065	50	1,019.0 (8)	637.9 (5)	249.9 (4)	23.51±0.09

Values in parentheses are absolute analytical errors. Uncertainties in age are calculated using error propagation and include uncertainties in the Re decay constant (0.31%), ^{185}Re (0.08%), and ^{190}Os (0.15%) spike calibration, weighting, and analytical errors. All errors reported at 2-σ levels

ity of spatially associated early Oligocene intrusions (U-Pb zircon ages of 36.0±0.2, 35.8±0.2, and 35.77±0.06 Ma, with a single intrusion dated at 15.75±0.04 Ma; Bineli Betsi 2007; Ponce 2011) are significantly older than the early Miocene Au-Ag mineralization hosted by Saraguro Group volcanic rocks (Bineli Betsi, 2007, obtained a ^{40}Ar/^{39}Ar plateau age of 18.9±0.5 Ma, possibly affected by Ar recoil, on sericite associated with the mineralization at Río Blanco).

The new geochronologic data presented in this study, substantiating and extending previously published K-Ar age data, demonstrate that porphyry Cu and porphyry-related epithermal mineralization in Ecuador intermittently spans the whole latest Oligocene to late Miocene period. Presently available geochronologic data for Tertiary mineral deposits in Ecuador are too scarce to draw any definite conclusions with respect to the possible occurrence of periods of particularly prolific porphyry Cu and porphyry-related mineralization. While a pilot study by Chiaradia et al. (2004) detected a preferential association of pre-late Miocene mineralization with non-adakitic arc magmatism in Ecuador, Schütte et al. (2010b), using a regionally more representative geochemical data set, show that subduction-related arc magmatism genetically associated with porphyry Cu deposit formation in Ecuador is not characterized by specific geochemical trace element signatures in general: it may be of both adakite-like or non-adakitic affinity (with the former trace element signature being particularly common since late Miocene times). At some porphyry Cu systems (Junín and Chaucha), porphyry intrusive parental melts probably evolved at higher pressure/greater crustal depth (indicated by adakite-like signatures) than parental melts of spatially associated precursor intrusions (Schütte et al. 2010b).

Systematic regional-scale, across-arc variations with respect to the timing of Miocene magmatism and mineralization are not observed in southern Ecuador (Fig. 3). Instead, both magmatism and metallogenesis may span the whole width (up to 100 km) of the arc segment at a given time. This observation is in line with similar observations by Noble et al. (2004) for the neighboring Miocene metallogenic belt of northern-central Peru. The timing of mineralization may differ significantly in a given region within the Miocene metallogenic belt of Ecuador. For example, the Gaby-Papa Grande and Chaucha porphyry systems, located at ca. 40 km distance to each other, formed at ca. 20 and 10 Ma, respectively (Fig. 3).

Geodynamic and tectonic impacts on Miocene mineralization and magmatism in Ecuador

The concentrated occurrence of Miocene porphyry Cu and porphyry-related mineral deposits in southern Ecuador, compared to a lower number of these deposits in northern Ecuador (where they are limited to the Western Cordillera, west of the late Miocene to recent volcanic deposits)

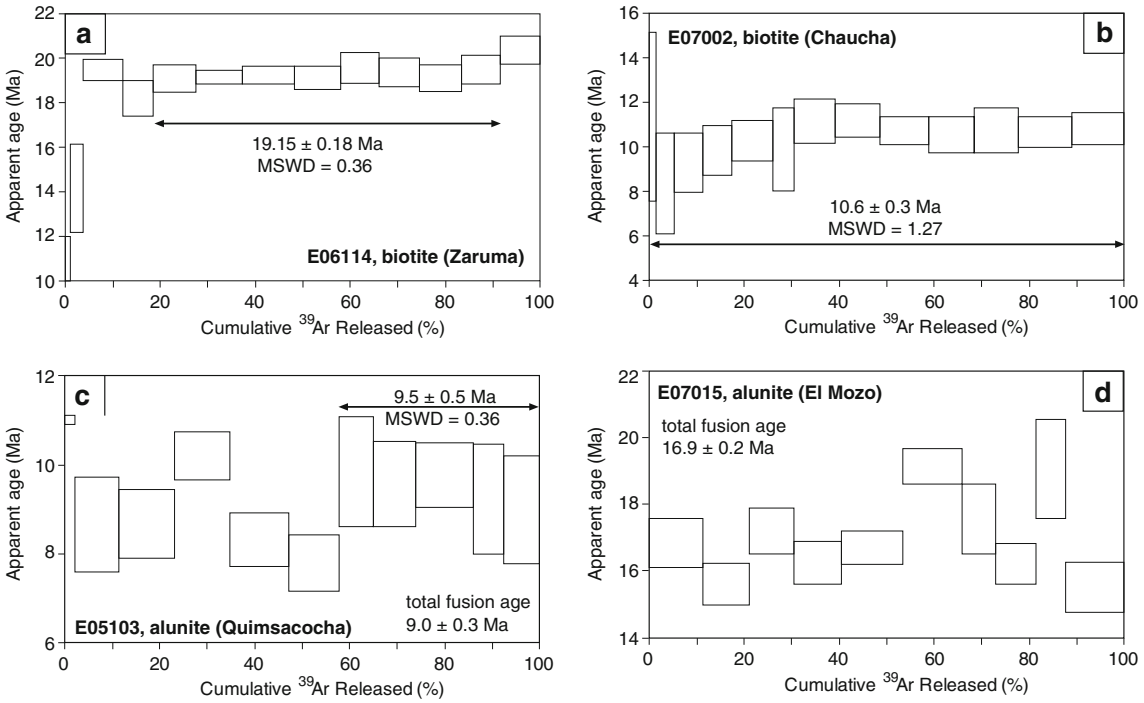

Fig. 10 $^{40}Ar/^{39}Ar$ release patterns for biotite and alunite analyzed in this study. **a** Hydrothermal biotite (potassic alteration; Zaruma); in order to allow adequate scaling of the apparent age axis, the first heating step has been cut off at 10 Ma (*error bar* extends down to 2 Ma). **b** Magmatic biotite (potassic alteration; Chaucha); as thermal resetting might not have been complete, the obtained 10.6±0.3 Ma plateau age represents a maximum age for cooling following the high-temperature, potassic hydrothermal alteration event affecting this sample (see text for discussion). **c** Alunite (advanced argillic alteration; Quimsacocha); the apparent age plateau at 9.5±0.5 Ma represents only 42% of the total ^{39}Ar released such that it does not present an acceptable plateau age (requiring >50% of total ^{39}Ar released); however, this age overlaps within error with the total fusion age of 9.0±0.3 Ma, such that these ages may serve as first-order maximum age estimates for cooling following advanced argillic alteration. **d** Alunite (advanced argillic alteration; El Mozo); the total fusion age of 16.9±0.2 Ma probably does not accurately indicate the timing of cooling following advanced argillic alteration as it predates the emplacement age of an altered porphyry dike at depth (16.04±0.04 Ma; U-Pb zircon; Schütte et al. 2010a). We consider a previously obtained age of 15.4±0.7 Ma (K-Ar alunite; PRODEMINCA 2000b) to approximate the timing of cooling following advanced argillic alteration at El Mozo more accurately. Data from Table 4; all errors reported at 2-σ levels

inversely correlates with the along-arc distribution of post-mineralization (late Miocene to recent) volcanic cover sequences in Ecuador (Fig. 2) which potentially conceal Miocene mineralization at depth (Chiaradia et al. 2004). The regional-scale localization of post-mineralization arc volcanism in Ecuador (and thus the potential accessibility to outcropping Miocene mineralization) may be broadly correlated with the subducting slab geometry. Mid- to late Miocene slab flattening, possibly related to the subduction of the inferred Inca oceanic plateau, resulted in the progressive cessation of arc volcanism along the southern Ecuadorian margin and, thus, the absence of areally extensive post-mineralization volcanic cover sequences (Figs. 1 and 2; Gutscher et al. 1999b; Schütte et al. 2010a). In northern Ecuador, on the other hand, productive arc volcanism continues to the present day; rather minor slab shallowing (instead of slab flattening), probably influenced by Carnegie Ridge seamount chain subduction, took place resulting in late Miocene eastward frontal arc migration and arc broadening (Schütte et al. 2010a). Carnegie Ridge collision at the Ecuadorian margin in late Miocene times does not seem to have any significant direct impact on Miocene metallogenesis (Fig. 12; also note that there is a lag time of few m.y. between initial ridge collision at the margin and subsequent slab shallowing/arc migration as a consequence of sustained ridge subduction).

In southern Ecuador, Miocene metallogenesis comprises both porphyry Cu and epithermal systems (Fig. 3). While epithermal mineral deposits are mostly hosted by Oligocene to Miocene volcanic rocks, porphyry Cu systems are often spatially associated (at the deposit to district scale) with large intrusive centers and older basement units (Table 1; Fig. 3) indicating uplift and exhumation. For a number of porphyry Cu deposits, there is a broad temporal correlation between periods of porphyry Cu mineralization and the inferred onset of compressive or transpressive pulses at a regional to local scale (Fig. 12). For example, Hungerbühler et al. (2002) infer a compressive–transpressive tectonic

Table 4 Analytical results of alunite and biotite Ar isotopic analyses of Miocene Ecuadorian mineral deposits

Step	$^{36}Ar/^{39}Ar$	$^{37}Ar/^{39}Ar$	$^{38}Ar/^{39}Ar$	$^{40}Ar^*/^{39}Ar$	$^{40}Ar^*$ [%]	cumulative ^{39}Ar [%]	Age±2-σ [Ma]	
Biotite (magmatic), potassic alteration, Chaucha (E07002), J=0.0008075±0.0000008								
1	0.0238	0.0000	0.0000	7.78	52.51	1.71	11.29	±3.78
2	0.0187	0.0000	0.0000	5.71	50.76	3.79	8.30	±2.26
3	0.0129	0.4912	0.0000	6.38	62.61	6.08	9.27	±1.36
4	0.0093	0.4457	0.0012	6.70	70.84	5.97	9.74	±1.14
5	0.0051	0.2504	0.0000	7.06	82.29	8.67	10.25	±0.96
6	0.0064	0.0000	0.0001	6.76	78.03	4.50	9.82	±1.88
7	0.0042	0.0000	0.0000	7.66	86.18	8.70	11.13	±1.00
8	0.0027	0.0000	0.0008	7.66	90.67	9.54	11.12	±0.74
9	0.0042	0.2958	0.0037	7.37	85.51	10.12	10.70	±0.63
10	0.0043	0.0000	0.0035	7.21	84.97	9.54	10.47	±0.80
11	0.0042	0.0046	0.0030	7.37	85.56	9.38	10.70	±0.98
12	0.0057	0.0000	0.0000	7.30	81.18	11.14	10.61	±0.67
13	0.0039	0.1391	0.0034	7.42	86.69	10.85	10.77	±0.74
Plateau: steps 1–13; 100% of total released ^{39}Ar								
Biotite (hydrothermal), potassic alteration, Zaruma (E06114), J=0.0008091±0.0000008								
1	0.0736	0.0000	0.0099	4.62	17.52	1.09	6.73	±5.20
2	0.0518	0.3440	0.0093	9.68	38.72	2.70	14.07	±1.99
3	0.0142	0.1730	0.0055	13.34	76.07	8.47	19.37	±0.52
4	0.0255	0.2206	0.0053	12.46	62.30	6.30	18.10	±0.80
5	0.0200	0.1303	0.0054	13.09	68.90	9.01	19.00	±0.62
6	0.0175	0.2087	0.0058	13.13	71.75	9.73	19.07	±0.34
7	0.0163	0.2150	0.0050	13.21	73.26	11.10	19.17	±0.39
8	0.0182	0.1993	0.0037	13.13	70.93	9.61	19.06	±0.52
9	0.0130	0.0000	0.0026	13.41	77.73	8.20	19.47	±0.70
10	0.0147	0.0000	0.0058	13.28	75.29	8.43	19.29	±0.66
11	0.0160	0.0000	0.0023	13.12	73.53	8.92	19.05	±0.56
12	0.0149	0.0000	0.0028	13.39	75.27	8.10	19.43	±0.63
13	0.0142	0.0728	0.0014	13.98	76.91	8.32	20.29	±0.62
Plateau: steps 5–12; 73% of total released ^{39}Ar								
Alunite, advanced argillic alteration, Quimsacocha (E05103), J=0.003999±0.000004								
1	0.0000	1.7986	0.0008	1.52	99.93	2.17	10.96	±0.06
2	0.0012	0.6409	0.0005	1.19	77.19	9.35	8.55	±1.03
3	0.0014	0.0000	0.0004	1.20	74.65	11.80	8.61	±0.77
4	0.0014	0.0000	0.0003	1.40	76.75	11.48	10.08	±0.56
5	0.0017	0.0000	0.0009	1.14	69.52	12.33	8.21	±0.58
6	0.0020	0.0000	0.0005	1.07	64.97	10.65	7.72	±0.61
7	0.0014	1.2334	0.0014	1.35	76.79	7.30	9.71	±1.24
8	0.0017	0.7593	0.0014	1.32	72.59	8.70	9.48	±0.96
9	0.0020	0.0000	0.0008	1.34	69.32	12.32	9.67	±0.77
10	0.0021	0.0000	0.0005	1.27	67.63	6.33	9.15	±1.23
11	0.0021	0.2786	0.0002	1.24	66.97	7.57	8.92	±1.26
Plateau: steps 7–11; 42% of total released ^{39}Ar								
Alunite, advanced argillic alteration, El Mozo (E07015), J=0.003999±0.000004								
1	0.0022	0.4081	0.0010	2.34	78.44	11.36	16.78	±0.69
2	0.0021	0.0000	0.0005	2.17	77.51	9.77	15.57	±0.61
3	0.0019	0.0000	0.0003	2.39	81.21	9.43	17.13	±0.70
4	0.0021	0.0000	0.0008	2.26	78.43	9.94	16.20	±0.64
5	0.0010	0.0000	0.0007	2.31	88.97	12.92	16.61	±0.51

Table 4 (continued)

Step	$^{36}Ar/^{39}Ar$	$^{37}Ar/^{39}Ar$	$^{38}Ar/^{39}Ar$	$^{40}Ar^*/^{39}Ar$	$^{40}Ar^*$ [%]	cumulative ^{39}Ar [%]	Age±2-σ [Ma]	
6	0.0012	0.0000	0.0011	2.65	88.27	12.61	19.04	±0.54
7	0.0015	0.0000	0.0005	2.44	84.68	6.98	17.51	±1.03
8	0.0020	0.0000	0.0006	2.26	79.02	8.67	16.21	±0.61
9	0.0024	0.0000	0.0010	2.65	78.53	6.04	19.01	±1.45
10	0.0024	0.2724	0.0009	2.16	75.60	12.28	15.48	±0.74

Plateau: none

event at 10–9 Ma (bringing about changes in the sedimentation setting of southern-central Ecuador) coinciding in time with porphyry Cu mineralization at Chaucha; the opening of the Inter-Andean Depression in a transpressive setting in northern Ecuador at ca. 6 Ma (Winkler et al. 2005) broadly correlates in time with porphyry Cu mineralization at Junín. Some authors (e.g., Sillitoe 1998; Perelló et al. 2003; Sillitoe and Perelló 2005) suggest that, among other factors, a compressive upper-crustal stress regime may positively impact on the formation of large porphyry Cu deposits due to its potential bearing on upper-crustal magma emplacement processes. In addition, Richards (2003) notes that mild, rather than strong compressive stress should be more favorable for porphyry Cu deposit formation in general, since arc magmas tend to preferentially pool at deeper crustal levels otherwise.

Metal endowment of the Miocene metallogenic belt of Ecuador relative to neighboring arc segments

The Miocene metallogenic and arc magmatic belts of Ecuador and northern-central Peru are broadly continuous in map view and share a number of similar characteristic features including the tectonomagmatic environment as well as the timing of mineralization (Fig. 2; Table 6; Sillitoe and Perelló 2005). Despite these similarities, the known metal endowment of the northern-central Peruvian Miocene metallogenic belt, including giant Au (e.g., Yanacocha, Lagunas Norte) and Cu deposits (e.g., La Granja), exceeds by far the metal endowment of its coeval Ecuadorian counterpart. Sillitoe (2008) notes that the underlying causes for the predisposition of specific arc segments with respect to their metal endowment are uncertain and may vary among different metals. Possible control factors include metal pre-enrichments and the prevailing redox state which might both impact on metallogenically favorable preconditioning of porphyry parental melts in the mantle wedge, in the sub-continental lithospheric mantle region, or in the lower crust (Sillitoe 2008, and references therein).

It might be speculated that accretion and broadscale underthrusting of exotic oceanic plateau crust in Ecuador (north of the Piñas-Portovelo fault; Fig. 3) since late Cretaceous times influenced some of these potential control parameters as this feature separates the Miocene metal-

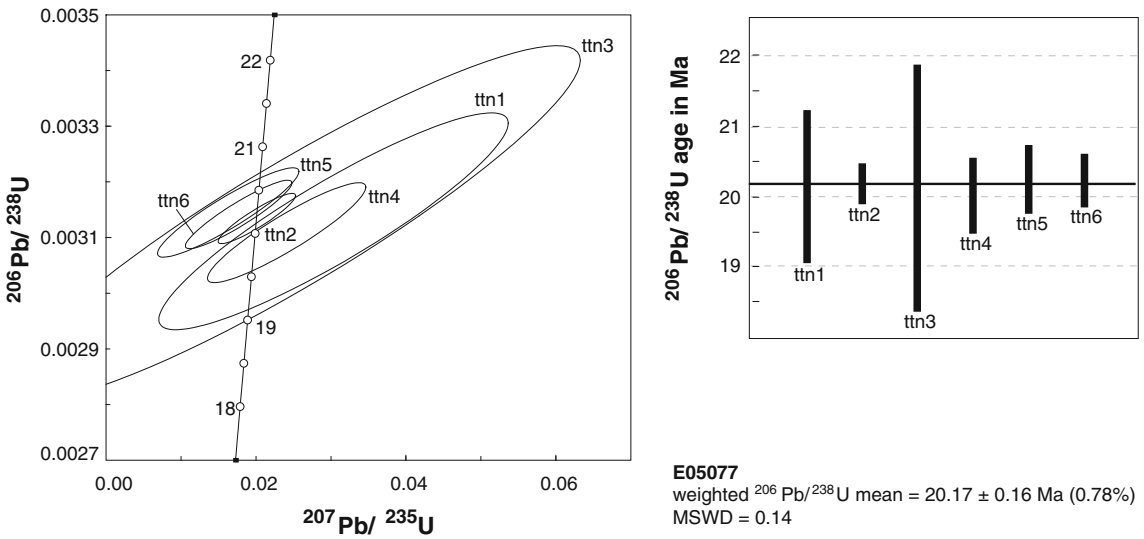

Fig. 11 Concordia plot and weighted mean $^{206}Pb/^{238}U$ average age for hydrothermal titanite related to sodic–calcic alteration at the Gaby-Papa Grande porphyry Au system. All errors reported at 2-σ levels

Table 5 U-Pb TIMS data for hydrothermal titanite at the Gaby-Papa Grande porphyry Au deposit

ID	Weight[mg]	Concentrations			Th/U[a]	Atomic ratios							rho	Apparent ages [Ma]					
		U [ppm]	Pb [ppm]	Pb_c [pg]		206/204[b]	207/206[c,d]	±2-σ [%]	207/235[c]	±2-σ [%]	206/238[c,d]	±2-σ [%]		206/238	±2-σ	207/235	±2-σ	207/206	±2-σ
ttn1	0.0512	32.8	0.39	52.6	1.1	24.3	0.0703	58	0.0303	63	0.00313	5.1	0.90	20.14	1.0	30.35	19.0	937.71	546
ttn2	0.0636	31.3	0.35	23.1	1.6	35.3	0.0466	20	0.0201	21	0.00313	1.2	0.91	20.17	0.2	20.22	4.2	26.23	5
ttn3	0.0101	28.6	0.31	12.3	0.9	22.6	0.0581	117	0.0250	125	0.00312	8.4	0.92	20.11	1.7	25.08	31.3	531.63	624
ttn4	0.0181	32.8	0.34	9.8	1.1	29.9	0.0562	34	0.0241	36	0.00311	2.4	0.91	20.01	0.5	24.17	8.7	460.27	155
ttn5	0.0115	30.0	0.35	5.6	1.9	30.4	0.0376	45	0.0163	47	0.00315	2.1	0.92	20.24	0.4	16.41	7.8	−515.58	−234
ttn6	0.0231	41.9	0.40	11.4	1.5	35.0	0.0408	31	0.0177	33	0.00314	1.6	0.92	20.22	0.3	17.80	5.8	−298.19	−94

[a] Calculated on the basis of radiogenic $^{208}Pb/^{206}Pb$ ratios, assuming concordancy

[b] Corrected for fractionation and spike

[c] Corrected for fractionation, spike, blank, and common lead (Stacey and Kramers 1975)

[d] Corrected for initial Th disequilibrium using an estimated Th/U ratio of 4

logenic belt of Ecuador from the higher endowed Peruvian belt in along-arc dimension. However, broadly coeval accretion of the same oceanic plateau at the neighboring Colombian margin to the north (Vallejo et al. 2009) did not result in a major metallogenic disruption there; giant Miocene Au deposits do exist in Colombia (e.g., La Colosa; Fig. 2) excluding this possibility as the principal control factor (Sillitoe 2008). The same consideration principally applies to any potential metallogenic impact of along-arc compositional differences in slab material (i.e., Farallon vs. Nazca crust of different age) subducted at the Colombian, Ecuadorian, and Peruvian margins (Fig. 1; Table 6). Other tectonomagmatic factors potentially supporting the formation of high-tonnage porphyry Cu deposits, such as periods of broadly compressive to transpressive stress and crustal thickening, possibly in association with a flat slab segment (e.g., Sillitoe 1998; Sillitoe and Perelló 2005; Sillitoe 2010), do not differ significantly between northern-central Peru and southern Ecuador (Table 6).

Differences in terms of Miocene metallogenesis in Ecuador and northern-central Peru mainly relate to shallow-crustal or surface-related features which may potentially influence primary and secondary processes of mineral deposit formation and preservation. In particular, the widespread occurrence of reactive limestone host units accounts for the abundant occurrence of skarn deposits in Peru (e.g., Noble and McKee 1999), compared to their scarcity in Ecuador; due to their impermeable nature, limestone host units may also focus fluid flow resulting in high-grade, hypogene porphyry-style mineralization (e.g., Sillitoe 2010). Thus, it may be speculated that the apparent lack of giant ore deposits associated with the Miocene metallogenic belt of Ecuador partly relates to shallow-crustal processes and, otherwise, is rather fortuitous, with no fundamental metallogenic factors disfavoring mineralization in this arc segment.

Conclusions

Hydrothermal mineralization and alteration events at ten Miocene Ecuadorian porphyry Cu and porphyry-related mineral deposits—constrained by molybdenite Re-Os, biotite and alunite $^{40}Ar/^{39}Ar$, and titanite U-Pb geochronology—substantiate and extend previously obtained K-Ar ages on these deposits. Alteration and mineralization events, covering a total age range of 23.5–6.1 Ma, closely correlate in time and space with porphyry intrusion emplacement (constrained by zircon U-Pb dating; Schütte et al. 2010a) at most deposits, and occurred in the same period as similar events in the neighboring metallogenic belt segment of northern-central Peru (and elsewhere in the Andes; Sillitoe and Perelló 2005). Several Miocene

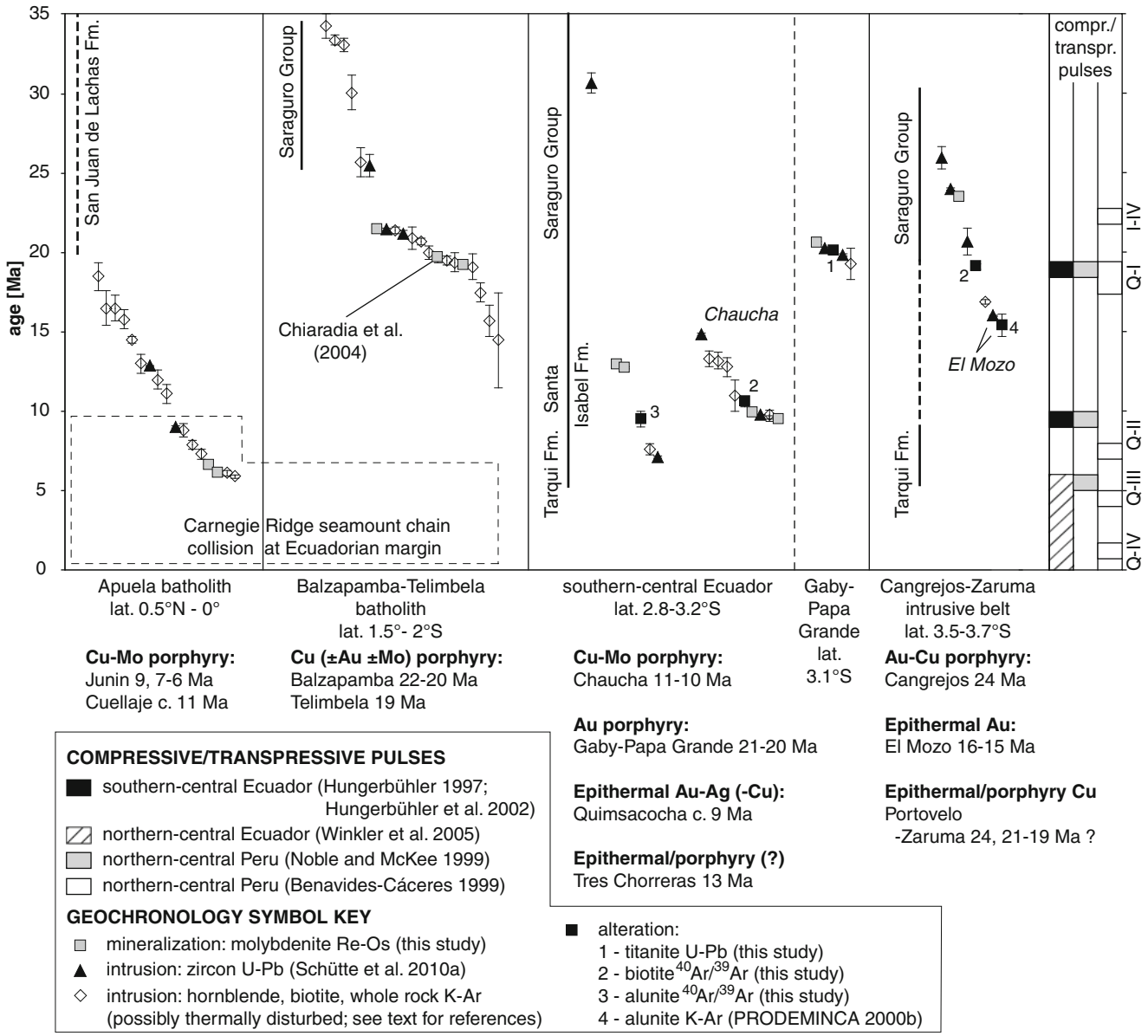

Fig. 12 Radiometric age distribution of magmatic and hydrothermal events at porphyry Cu and porphyry-related mineral deposits and spatially associated Oligocene–Miocene plutons in specific segments of the Miocene metallogenic belt of Ecuador. Age ranges for volcanic formations in southern-central Ecuador (Saraguro Group, Santa Isabel Formation, Tarqui Formation; Fig. 3) are indicated by *vertical lines* (*dashed* where geochronologic control is weak); andesites of the San Juan de Lachas Formation, exposed locally in the Western Cordillera of northern Ecuador, are broadly coeval with the Saraguro Group in southern-central Ecuador. Note that late Miocene to recent arc volcanism in northern-central Ecuador (east of the Western Cordillera) is not shown. *Dashed hairline box* indicates the region (in space and time) where the Carnegie Ridge seamount chain collides with the Ecuadorian margin. Also shown are local- to regional-scale, transpressive or compressive pulses described for Ecuador and northern-central Peru (*I* Inca, *Q* Quechua; note that the minimum size of boxes, corresponding to 1 m.y., was chosen for better illustration; the actual minimum duration of individual events might be shorter). See text for discussion on relationship of porphyry Cu mineralization, spatio-temporal distribution of arc volcanism, compressive–transpressive pulses, and Carnegie Ridge subduction. Intrusive and volcanic age references are compiled in Schütte et al. (2010a)

porphyry Cu deposits in Ecuador are spatially associated with batholith-scale precursor intrusive centers assembled over ≥5 m.y. time periods. In a given area, these porphyry systems tend to be associated with the youngest magmatic event, postdating major batholith construction at a regional scale. At some deposits, porphyry Cu mineralization broadly correlates in time with the onset of local- to regional-scale, transpressive or compressive pulses. Systematic along- or across-arc age distribution trends are not observed for Miocene Ecuadorian mineral deposits.

Table 6 Comparison of geological features of the Miocene metallogenic belts of Ecuador and northern-central Peru

	Northern-central Peru	Southern Ecuador	Northern-central Ecuador	Ref.
Main commodities	Au, Cu, base metals	Au, Cu	Cu	1–3
Main mineral deposit types	porphyry Cu-Mo, porphyry Au-Cu, high-sulfidation epithermal, Cordilleran vein, replacements, skarn	porphyry Cu-Mo, porphyry (Cu-) Au, high-, intermediate-, low-sulfidation epithermal	porphyry Cu-Mo	1–3
Mineralization age range	23–6 Ma	24–9 Ma	21–20 Ma, 9–6 Ma	1–3; this study
Mineralization peaks	15–13 Ma; 8–7 Ma	Not enough data available to evaluate	Not enough data available to evaluate	1–2
Recorded compressive/ transpressive pulses	Inca IV (22 Ma), Quechua I (19–17 Ma), Quechua II (ca. 9 Ma or 8–7 Ma), Quechua III (ca. 6 or 5–4 Ma), Quechua IV (ca. 2 Ma)	19 Ma; 10–9 Ma	since ca. 6 Ma	1, 4, 5–7
Present-day slab geometry	Flat slab	Flat slab	ca. 25–35° subduction angle	8, 9
Subducted oceanic lithosphere type	Farallon crust (>30 Ma)	Farallon crust (>30 Ma)	Nazca crust (ca. 10–23 Ma); mostly carrying Carnegie Ridge seamounts	10
Main host lithologies of mineral deposits	Mesozoic shelf carbonates and sediments	Paleozoic to Mesozoic metasediments	Late Cretaceous to Paleogene island arc volcanic–volcaniclastic rocks	1, 11
	Neogene volcanic rocks and intrusions	Neogene volcanic rocks and intrusions	Neogene intrusions	
Deep-crustal basement units	Mature continental crust	Oceanic plateau ± continental crust (north of Cangrejos-Zaruma intrusive belt) Continental crust (south of Cangrejos-Zaruma intrusive belt)	Oceanic plateau crust (Western Cordillera)	1, 11

References: 1—Noble and McKee (1999), 2—Noble et al. (2004), 3—PRODEMINCA (2000a), 4—Benavides-Cáceres (1999), 5—Hungerbühler (1997), 6—Hungerbühler et al. (2002), 7—Winkler et al. (2005), 8—Gutscher et al. (1999b), 9—Guillier et al. (2001), 10—Lonsdale (2005), 11—Vallejo et al. (2009)

At a regional scale, Miocene porphyry Cu and porphyry-related mineralization is preferentially exposed in the principal Tertiary arc region of southern Ecuador where areally extensive post-mineralization (late Miocene to recent) volcanic cover sequences are lacking. In northern Ecuador, outcrops of porphyry Cu mineralization are limited to the Western Cordillera and its western foothills, west of the present-day axis of the productive volcanic arc. The along-arc variation in the distribution of post-mineralization volcanic sequences (and its influence on the outcropping features of Miocene mineral deposits) is related to the establishment of an amagmatic flat slab segment since mid- to late Miocene times that transgresses southern Ecuador and neighboring northern Peru. Despite of sharing a number of similarities with respect to the tectonomagmatic and metallogenic environment, the known metal endowment of the Miocene metallogenic belt segment in southern Ecuador lags behind that of the coeval belt in northern-central Peru. However, the Au endowment of the Miocene metallogenic belt of Colombia to the north indicates that the tectonomagmatic and metallogenic setting of the northern Andes is also amenable to giant deposit formation.

Acknowledgments We thank Aldo Bendezú Juarez, Miguel Ponce, Richard Spikings, and Kalin Kouzmanov for stimulating discussions, Blair Schoene for the advice on titanite column chemistry preparation, Pato Salazar for the support in the field, and Melissa Ortelli for the analytical support with Raman spectroscopy. The manuscript benefited greatly from helpful reviews by José Perelló, an anonymous reviewer, and Robert Creaser, as well as from the thoughtful editorial handling by Patrick Williams. Field work in Ecuador in the 2006–2007 period benefited from the logistic support of Ascendant Copper, International Minerals Corporation, Dynasty Metals & Mining, Iamgold, AtlasMoly, Channel Resources, and Ecuagold, and we gratefully acknowledge valuable discussions with staff members of these companies. PS benefited from travel grants by the Augustin Lombard Foundation of the Geneva SPHN Society and the Ecole Doctorale en Sciences des Minéraux (EDSM). This project was supported by the Swiss National Science Foundation (grants 200021-109636 and 200020-117617).

References

Barra F, Ruiz J, Mathur R, Titley S (2003) A Re-Os study on sulfide minerals from the Bagdad porphyry Cu-Mo deposit, northern Arizona, United States. Mineral Deposita 38:585–596

Barra F, Ruiz J, Valencia VA, Ochoa-Landín L, Chesley JT, Zurcher L (2005) Laramide porphyry Cu-Mo mineralization in northern Mexico: age constraints from Re-Os geochronology in molybdenite. Econ Geol 100:1605–1616

Beate B, Monzier M, Spikings R, Cotton J, Silva J, Bourdon E, Eissen JP (2001) Mio-Pliocene adakite generation related to flat subduction in southern Ecuador: the Quimsacocha volcanic center. Earth Planet Sci Lett 192:561–570

Benavides-Cáceres V (1999) Orogenic evolution of the Peruvian Andes: the Andean cycle. In: Skinner BJ (ed.) Geology and ore deposits of the central Andes. SEG Special Publ 7:61–107

Bineli Betsi T (2007) The low-sulfidation Au-Ag deposit of Rio Blanco (Ecuador): geology, mineralogy, geochronology and isotope geochemistry. M.Sc. thesis, Université de Genève

Chesley J (1999) Integrative geochronology of ore deposits: new insights into the duration and timing of hydrothermal circulation. In: Lambert DD, Ruiz J (eds) Application of radiogenic isotopes to ore deposit research and exploration. Rev Econ Geol 12:115–141

Chiaradia M, Fontboté L, Beate B (2004) Cenozoic continental arc magmatism and associated mineralization in Ecuador. Mineral Deposita 39:204–222

Chiaradia M, Vallance J, Fontboté L, Stein H, Schaltegger U, Coder J, Richards J, Villeneuve M, Gendall I (2009) U-Pb, Re-Os, and $^{40}Ar/^{39}Ar$ geochronology of the Nambija Au-skarn and Pangui porphyry Cu deposits, Ecuador: implications for the Jurassic metallogenic belt of the Northern Andes. Mineral Deposita 44:371–387

Corriente Resources Inc. (2008) Mirador copper-gold project—30,000 TPD feasibility study. Corriente Resources. http://www.corriente.com/media/PDFs/news/technical_reports/MIRADOR_30K_Report_FINAL_SEDAR.pdf. Accessed 1 June 2011

Creaser RA, Papanastassiou DA, Wasserburg GJ (1991) Negative thermal ion mass spectrometer of Os, Re and Ir. Geoch Cosmoch Acta 55:397–401

Daly MC (1989) Correlation between Nazca/Farallon plate kinematics and forearc basin evolution in Ecuador. Tectonics 8:769–790

Dunkley PN, Gaibor A (1997) Mapa geológico de la Cordillera Occidental del Ecuador entre 2°–3° S, escale 1/200.000. CODIGEM-BGS, Quito

Ego F, Sébrier M, Lavenu A, Yepes H, Egues A (1996) Quaternary state of stress in the Northern Andes and the restraining bend model for the Ecuadorian Andes. Tectonophysics 259:101–116

Goossens PJ, Hollister VF (1973) Structural control and hydrothermal alteration pattern of Chaucha porphyry copper, Ecuador. Mineral Deposita 8:321–331

Guillier B, Chatelain JL, Jaillard E, Yepes H, Poupinet G, Fels JF (2001) Seismological evidence on the geometry of the orogenic system in central-northern Ecuador (South America). Geophys Res Lett 28:3749–3752

Gustafson LB, Hunt JP (1975) The porphyry copper deposit at El Salvador, Chile. Ec Geol 70:857–912

Gustafson LB, Vidal CE, Pinto R, Noble DC (2004) Porphyry–epithermal transition, Cajamarca region, northern Peru. SEG Spec Publ 11:279–299

Gutscher MA, Malavieille J, Lallemand S, Collot JY (1999a) Tectonic segmentation of the North Andean margin: impact of the Carnegie Ridge collision. Earth Planet Sci Lett 168:255–270

Gutscher MA, Olivet JL, Aslanian D, Eissen JP, Maury R (1999b) The "lost Inca Plateau": cause of flat subduction beneath Peru? Earth Planet Sci Lett 171:335–341

Hungerbühler D (1997) Tertiary basins in the Andes of southern Ecuador (3º00′–4º20′): sedimentary evolution, deformation and regional tectonic implications. PhD Thesis, Institute of Geology, ETH Zurich, Switzerland

Hungerbühler D, Steinmann M, Winkler W, Seward D, Egüez A, Peterson DE, Helg U, Hammer C (2002) Neogene stratigraphy and Andean geodynamics of southern Ecuador. Earth Sci Rev 57:75–124

Iamgold (2009) Quimsacocha Gold Project, Azuay Province, Ecuador. Technical Report, available on http://www.sedar.com. Accessed on 29 September 2009

IBM (2005) Technical Report El Mozo Property, Cochapata and Morasloma, Azuay Province, Southern Ecuador. Technical Report, available on http://www.sedar.com. Accessed on 4 September 2007

Jaffey A, Flynn K, Glendenin L, Bentley W, Essling A (1971) Precision measurement of half-lives and specific activities of 235U and 238U. Phys Rev Ser C4:1889–1906

James DE, Sacks IS (1999) Cenozoic formation of the central Andes: a geophysical perspective. In: Skinner BJ (ed.) Geology and ore deposits of the central Andes. Soc Econ Geol Special Publ 7:1–25

Kay SM, Mpodozis C, Coira B (1999) Neogene magmatism, tectonism, and mineral deposits of the Central Andes (22° to 33° S latitude). SEG Special Publ 7:27–59

Kinross Gold Corporation (2010) Fruta del Norte Project, Ecuador, NI 43–101 Technical Report. Kinross Gold Corporation. http://www.kinross.com/media/98356/fdn%20technical%20report.pdf. Accessed on 1 June 2011

Knight KB, Renne PR, Halkett A, White N (2003) $^{40}Ar/^{39}Ar$ dating of the Rajahmundry Traps, Eastern India and their relationship to the Deccan Traps. Earth Planet Sci Lett 208:85–99

Koppers AAP (2002) ArArCALC—software for $^{40}Ar/^{39}Ar$ age calculations. Comput Geosci 28:605–619

Kuiper YD (2002) The interpretation of inverse isochron diagrams in $^{40}Ar/^{39}Ar$ geochronology. Earth Planet Sci Lett 203:499–506

Litherland M, Aspden JA, Jemielita RA (1994) The metamorphic belts of Ecuador. Overseas Memoir 11. BGS, Keyworth

Lonsdale P (2005) Creation of the Cocos and Nazca plates by fission of the Farallon Plate. Tectonophysics 404:237–264

Lonsdale P, Klitgord KD (1978) Structure and tectonic history of the eastern Panama basin. Geol Soc Am Bull 89:981–999

Ludwig K (2003) Isoplot 3.00. Berkeley Geochronology, vol 4. Center Special Publ 4, Berkeley, California

McNulty BA, Farber DL, Wallace GS, Lopez R, Palacios O (1998) Role of plate kinematics and plate-slip-vector partitioning in continental magmatic arcs: evidence from the Cordillera Blanca, Peru. Geology 26:827–830

Mégard F (1984) The Andean orogenic period and its major structures in central and northern Peru. J Geol Soc Lond 141:893–900

Melling DR, Schultz D, Allen DG (2007) Technical report on the Tres Chorreras polymetallic copper-molybdenum-gold-silver project, Azuay province, Ecuador. Technical Report, available on http://www.sedar.com. Accessed 19 February 2008

MICON (2005a) Technical report—review of the quartz porphyry-hosted copper-molybdenum mineralisation at Junín, Otavalo, Ecuador. Technical Report, available on http://www.sedar.com. Accessed 23 June 2006

MICON (2005b) Technical report—review of the quartz porphyry-hosted copper-molybdenum mineralisation at Chaucha, Cuenca,

Ecuador. Technical Report, available on http://www.sedar.com. Accessed 26 June 2006
MMAJ/JICA (1991) Report on the mineral exploration in the Bolivar area, Republic of Ecuador. Consolidated report no. 6 (MPN, CR (3), 91–72). Metal Mining Agency of Japan and Japan International Cooperation Agency, Tokyo
MMAJ/JICA (1998) Informe final sobre la exploración mineral de cooperación técnica en el area de Imbaoeste, República del Ecuador. Consolidated report no. 4 (MPN, JR, 98–088). Metal Mining Agency of Japan and Japan International Cooperation Agency, Tokyo
Noble DC, McKee EH (1999) The Miocene metallogenic belt of central and northern Peru. SEG Special Publ 7:155–193
Noble DC, Vidal CE, Perelló J, Rodríguez OP (2004) Space–time relationships of some porphyry Cu-Au, epithermal Au, and other magmatic-related mineral deposits in northern Peru. SEG Spec Publ 11:313–318
Perelló J, Carlotto V, Zárate A, Ramos P, Posso H, Neyra C, Caballero A, Fuster N, Muhr R (2003) Porphyry-style alteration and mineralization of the middle Eocene to early Oligocene Andahuaylas-Yauri belt, Cuzco region, Peru. Econ Geol 98:1575–1605
Ponce M (2011) Geochronology and geochemistry of igneous rocks hosting the low-sulfidation gold-silver deposit of Río Blanco (Ecuador). M.Sc. thesis, Université de Genève
Potter M (2004) Summary report on the Cangrejos property, Southwest Ecuador. Technical report, available on http://www.sedar.com. Accessed 27 August 2007
Pratt WT, Figueroa JF, Flores BG (1997) Mapa geológico de la Cordillera Occidental del Ecuador entre 3°–4°S, escala 1/200.000. CODIGEM-BGS, Quito
Pratt WT, Duque P, Ponce M (2005) An autochthonous geological model for the eastern Andes of Ecuador. Tectonophysics 399:251–278
PRODEMINCA (2000a) Evaluación de distritos mineros del Ecuador, vol 4—Depósitos porfídicos y epi-mesotermales relacionados con intrusiones de las Cordilleras Occidental y Real. UCP PRODEMINCA Proyecto MEM BIRF, EC, Quito, pp 36–55
PRODEMINCA (2000b) Evaluación de distritos mineros del Ecuador, vol 2—Depósitos epitermales en la Cordillera Andina. UCP PRODEMINCA Proyecto MEM BIRF, EC, Quito, pp 36–55
PRODEMINCA (2000c) Evaluación de distritos mineros del Ecuador, vol 5—Depósitos porfídicos y epi-mesotermales relacionados con instrusiones de la Cordillera del Cóndor. UCP PRODEMINCA Proyecto MEM BIRF, EC, Quito, pp 36–55
Richards JP (2003) Tectono-magmatic precursors for porphyry Cu-(Mo-Au) deposit formation. Econ Geol 98:1515–1533
Salazar FP (2007) Geología, alteración y mineralización del pórfido de cobre-molibdeno Junín, Provincia de Imbabura, Ecuador. MSc thesis, Escuela Politecnica Nacional, Quito
Schmitz MD, Bowring SA (2001) U-Pb zircon and titanite systematic of the Fish Canyon Tuff: an assessment of high-precision U-Pb geochronology and its application to young volcanic rocks. Geoch Cosmoch Acta 65:2571–2587
Schütte P, Chiaradia M, Beate B (2010a) Geodynamic controls on Tertiary arc magmatism in Ecuador: Constraints from U–Pb zircon geochronology of Oligocene–Miocene intrusions and regional age distribution trends. Tectonophysics 489:159–176
Schütte P, Chiaradia M, Beate B (2010b) Petrogenetic evolution of arc magmatism associated with late Oligocene to late Miocene porphyry-related ore deposits in Ecuador. Econ Geol 105:1243–1270
Seedorff E, Dilles JH, Proffett JM Jr, Einaudi MT, Zurcher L, Stavast WJA, Johnson DA, Barton MD (2005) Porphyry deposits: characteristics and origin of hypogene features. Econ Geol 100th Anniversary Volume:251–298
Sillitoe RH (1972) A plate tectonic model for the origin of porphyry copper deposits. Econ Geol 67:184–197
Sillitoe RH (1988) Epochs of intrusion-related copper mineralization in the Andes. J South Am Earth Sci 1:89–108
Sillitoe RH (1998) Major regional factors favouring large size, high hypogene grade, elevated gold content and supergene oxidation and enrichment of porphyry copper deposits. In: Porter TM (ed) Porphyry and hydrothermal copper and gold deposits—a global perspective. Australian Mineral Foundation, Adelaide, pp 21–34
Sillitoe RH (2008) Major gold deposits and belts of the North and South American Cordillera: Distribution, tectonomagmatic settings, and metallogenic considerations. Econ Geol 103:663–687
Sillitoe RH (2010) Porphyry copper systems. Econ Geol 105:3–41
Sillitoe RH, Perelló J (2005) Andean copper province: tectonomagmatic settings, deposit types, metallogeny, exploration, and discovery. Econ Geol 100th Anniversary Volume:845–890
Smoliar MI, Walker RJ, Morgan JW (1996) Re-Os ages of group IIA, IIIA, IVA and IVB iron meteorites. Science 271:1099–1102
Snee LW (2002) Argon thermochronology of mineral deposits—a review of analytical methods, formulations, and selected applications. U.S. Geological Survey Bulletin 2194
Spencer RM, Montenegro JL, Gaibor A, Perez EP, Mantilla G, Viera F, Spencer CE (2002) The Portovelo-Zaruma mining camp, SW Ecuador: porphyry and epithermal environments. SEG Newsletter 49:8–14
Spikings RA, Winkler W, Seward D, Handler R (2001) Along-strike variations in the thermal and tectonic response of the continental Ecuadorian Andes to the collision with heterogeneous oceanic crust. Earth Planet Sci Lett 186:57–73
Spikings RA, Crowhurst PV, Winkler W, Villagomez D (2010) Syn- and post-accretionary cooling history of the Ecuadorian Andes constrained by their in-situ and detrital thermochronometric record. J South Am Earth Sc 30:121–133
Srivastava M, Steidtmann H, Gowans RM (2008) NI 43–101 Technical report on the preliminary feasibility study for the Gaby gold project, Ecuador. Technical Report, available on http://www.sedar.com. Accessed 26 May 2009
Stacey JS, Kramers JD (1975) Approximation of terrestrial lead isotope evolution by a two-stage model. Earth Planet Sci Lett 26:207–221
USGS (2009) 2007 Minerals Yearbook Ecuador (advance release). U.S. Geological Survey. http://minerals.usgs.gov/minerals/pubs/country/2007/myb3-2007-ec.pdf. Accessed 13 January 2011
Vallejo C, Winkler W, Spikings RA, Luzieux L, Heller F, Bussy F (2009) Mode and timing of terrane accretion in the forearc of the Andes in Ecuador. In: Kay SM, Ramos VA, Dickinson WR (eds.), Backbone of the Americas: Shallow Subduction, Plateau Uplift, and Ridge and Terrane Collision. Geol Soc Am Memoir 204
Winkler W, Villagomez D, Spikings R, Abegglen P, Tobler S, Eguez A (2005) The Chota basin and its significance for the inception and tectonic setting of the inter-Andean depression in Ecuador. J South Am Earth Sci 19:5–19
Witt C, Bourgois J, Michaud F, Ordoñez M, Jiménez N, Sosson M (2006) Development of the Gulf of Guayaquil (Ecuador) during the Quaternary as an effect of the North Andean block tectonic escape. Tectonics 25:TC3017